Optical studies of crystal phase heterostructures

Geijselaers, Irene

2021

Document Version:
Other version

Optical studies of crystal phase heterostructures

IRENE GEIJSELAERS
DEPARTMENT OF SOLID STATE PHYSICS | FACULTY OF ENGINEERING | LUND UNIVERSITY

Optical studies of crystal phase heterostructures

Optical studies of crystal phase heterostructures

by Irene Geijselaers

LUND
UNIVERSITY

DOCTORAL DISSERTATION
Thesis advisors: Prof. Mats-Erik Pistol, Dr. Sebastian Lehmann, Prof. Craig Pryor
Faculty opponent: Dr. Hannah Joyce

To be presented, with the permission of the Faculty of Engineering, LTH of Lund University, for public criticism in Rydbergsalen at the Department of Solid State Physics on Friday, the 22th of October 2021 at 13:15.

Organization
LUND UNIVERSITY
Department of Solid State Physics
Box 118
SE–221 00 LUND
Sweden

Document name
DOCTORAL DISSERTATION

Date of disputation
2021-10-22

Sponsoring organization

Author(s)
Irene Geijselaers

Title and subtitle
Optical studies of crystal phase heterostructures

Abstract
III-V semiconductors are commonly used for a variety of optical applications, such as LED based lights and solar sells. Most III-V semiconductors, such as GaAs and InP, exhibit the zinc-blende (zb) crystal structure, but in the form of nanowires it is also possible to create them in the wurtzite (wz) crystal structure. This allows for the creation of novel heterostructures consisting of the same compound, but different crystal structures, so called crystal phase or polytype heterostructures. Unlike material heterostructures, these polytype heterostructures have atomically sharp interfaces with minimal strain. This could make them ideal candidates for a number of applications, such as single photon sources, and as an environment to study interesting physical phenomena such as electron crystals and quantum dots (Q-dots).

In this work I have used photoluminescence (PL) spectroscopy and photoluminescence excitation (PLE) spectroscopy to investigate a number of InP and GaAs polytype heterostructures. PL and PLE are non-invasive optical techniques that use absorption and emission of photons to gain information about a number of semiconductor properties, such as bandgap, band structure and the energy of impurity levels. The PL and PLE measurements of single, nanowires are combined with electron microscopy. This allows for the correlation of the morphology and crystal structure quality with the optical properties of the polytype heterostructures. Finally, the measured optical properties are correlated to numerical calculations of electronic structure.

This thesis consists of three papers. In paper I it is shown that the Fermi-level pinning at the semiconductor-air surface influences the perceived valence band offset between the wz and zb crystal structure in GaAs nanowires. In paper II the existence of a two dimensional electron gas at the wz-zb interface in modulation doped InP nanowires is demonstrated. Finally, paper III explores zb-GaAs Q-dots in narrow wz-GaAs nanowires. The existence of multiple Q-dot states is confirmed trough PLE, whose energies correlate with numerical calculations of the Q-dot energy levels. The results in this thesis pave the way towards the use of polytype heterostructures for the study of physical phenomena, such as electron crystals.

Key words
III-V semiconductor nanowire, Photoluminescence, Photoluminescence excitation, Polytype, Crystal phase heterostructure, InP, GaAs, Wurtzite

Classification system and/or index terms (if any)

Supplementary bibliographical information

Language
English

ISSN and key title

ISBN
978-91-8039-002-6(print)
978-91-8039-003-3(pdf)

Recipient's notes

Number of pages
112

Price

Security classification

Optical studies of crystal phase heterostructures

by Irene Geijselaers

LUND
UNIVERSITY

Cover illustration front: An artistic rendition of power dependent photoluminescence spectra of a wurtzite-zinc-blende InP heterostructure.

Faculty of Engineering, LTH, Department of Solid State Physics

ISBN: 978-91-8039-002-6 (print)
ISBN: 978-91-8039-003-3 (pdf)

Printed in Sweden by Media-Tryck, Lund University, Lund 2021

"This extreme conception here may be wrong [...]"
- **E. Schrödinger**, 1926,
on the Schrödinger equation

Contents

Abstract i

Popular scientific description iii

List of papers vii

Acknowledgements ix

Abbreviations and symbols xi

1 Introduction 1

2 Background 5
- 2.1 Polytypism . . . 5
- 2.2 Semiconductor physics . . . 9
  - 2.2.1 Electronic band structure (and heterostructures) . . . 9
  - 2.2.2 Quantum confinement (and DOS) . . . 12
  - 2.2.3 Charge carrier generation and recombination . . . 14
- 2.3 Fermi-level pinning . . . 16
  - 2.3.1 Mathematical description . . . 19

3 Experimental methods 23
- 3.1 Nanowire growth . . . 23
- 3.2 Optical spectroscopy . . . 25
  - 3.2.1 Photoluminescence spectroscopy . . . 25
  - 3.2.2 Photoluminescence excitation spectroscopy . . . 27
- 3.3 Microscopy . . . 28
  - 3.3.1 Optical microscopy . . . 28
  - 3.3.2 Electron microscopy . . . 28
- 3.4 One-band effective mass calculations . . . 30
- 3.5 Sample preparation and procedures . . . 32

4 Results 35
- 4.1 Radial band bending in GaAs . . . 35
- 4.2 2DEG formation in polytype InP . . . 40
- 4.3 Crystal phase defined GaAs quantum dots . . . 44

5 Conclusions and outlook **49**

Bibliography **51**

Abstract

III-V semiconductors are commonly used for a variety of optical applications, such as LED based lights and solar sells. Most III-V semiconductors, such as GaAs and InP, exhibit the zinc-blende (zb) crystal structure, but in the form of nanowires it is also possible to create them in an additional crystal sturcture: the wurtzite (wz) crystal structure. This allows for the creation of novel heterostructures consisting of the same compound, but different crystal structures, so called crystal phase or polytype heterostructures. Unlike material heterostructures, which combine different compounds, polytype heterostructures have atomically sharp interfaces with minimal strain and are therefore ideal candidates for a number of applications, such as single photon sources, and as an environment to study interesting physical phenomena such as electron crystals and quantum dots (Q-dots).

In this work I have used photoluminescence (PL) spectroscopy and photoluminescence excitation (PLE) spectroscopy to investigate a number of InP and GaAs polytype heterostructures to examine their optical response. PL and PLE are non-invasive optical techniques that use absorption and emission of photons to gain information about a number of semiconductor properties, such as bandgap, band structure and the energy of impurity levels. The PL and PLE measurements of single, individual nanowires are combined with electron microscopy. This allows for the correlation of the morphology and crystal structure quality with the optical properties of the polytype heterostructures. Finally, the measured optical properties are correlated to numerical calculations of electronic structure for a complete exploration of the properties of polytype heterostructures.

The work in this thesis is presented in three papers. In paper I it is shown that the Fermi-level pinning at the semiconductor-air surface influences the perceived valence band offset between the wz and zb crystal structure in GaAs nanowires. In paper II the existence of a two dimensional electron gas at the wz-zb interface

in modulation doped InP nanowires is demonstrated. Finally, paper III explores zb-GaAs Q-dots in narrow wz-GaAs nanowires. The existence of multiple Q-dot states is confirmed trough PLE, whose energies correlate with numerical calculations of the Q-dot energy levels. The results in this thesis pave the way towards the use of polytype heterostructures for high electron mobility applications, Q-dot based photon sources and the study of physical phenomena, such as electron crystals.

Popular scientific description

What do the chips in your computer, the LED-based lights on your ceiling, and the solar cells on your roof have in common? They are all made out of semiconductor materials. Semiconductors are materials that only conduct current under certain circumstances and offer the possibility to finely tune when there is current, and how many electrons carry it. This is, for example, what allows the transistors (electronic switches) in your computer to turn on and off. In the search for technological advancement, scientists are constantly looking for better, faster and smaller combinations of semiconductors. In this thesis I research a relatively new selection of semiconductors, called polytype semiconductors, for possible applications.

Semiconductors, as the name suggests, only conduct current, under specific circumstances. The reason for this is the physical property called the *energy bands*. Semiconductor materials have bands of possible energy levels electrons can have. One can compare such a band to a box filled with marbles. A marble at the top of the box has more potential energy due to gravity than a marble at the bottom of the box. However it is impossible for the top marble to lose that energy since it is being supported by all the marbles below it. In a similar way electrons in an energy band have different energies due to being "stacked" on top of each other.

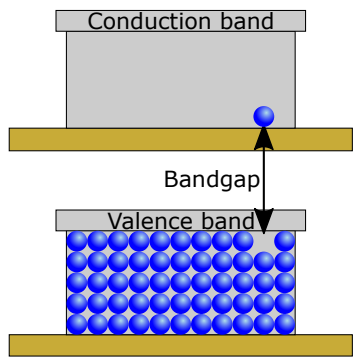

Figure 1: A box completely filled with marbles and a completely empty box. This is similar to energy bands in a semiconductor.

Now imagine two separate marble boxes on a shelf above each other, such as in figure 1. The bottom box is completely filled with marbles while the top box is completely empty. In

neither box is it possible for marbles to move in this scenario, since the top box is empty and the bottom box is so tightly packed with marbles that even if you tilt the box they are not able to move. However, if you would raise one marble from the bottom box to the top box, adding potential energy to that one marble, suddenly it would be possible for marbles to move. Not only that one marble in the top box can move, but also the hole in the bottom box can move, because of marbles filling up the space left where one was taken out.

This is similar to what happens to electrons in semiconductors. An electron gets raised from the completely filled *valence band* to the completely empty *conduction band*, leaving behind a hole. For this to happen the electron needs to get enough energy to overcome the so called *bandgap* between the two bands and it is not possible for the electron to exist within the bandgap. Usually the electron gains this energy through heat or light, or by an external voltage. It is possible for an electron to fall back over the bandgap into the hole it left behind and send out light with an energy that corresponds to the bandgap energy. This is the working principle of LED-based lights.

Sometimes it is advantageous to combine different semiconductors with different bandgaps to create so called *heterostructures*. This can be very difficult to do in practice because different materials have different interatomic distances. If you would build the bottom part of a house out of small bricks and the top part of a house out of large bricks, the interface between the bricks will look pretty weird, especially if you attempt to align the large bricks to the small bricks like in figure 2. This is similar to what happens when two materials with different atomic distances are combined: the interface will experience strain because the bricks don't fit. Another problem with combining different materials is that the interface will not be sharp. There can be some mixing of the materials, which gives rise to non-ideal interfaces.

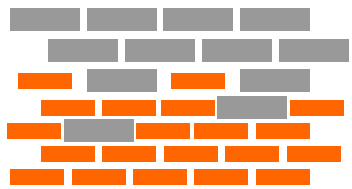

Figure 2: A brick wall using two different sizes brick and intermixing at the interface. This leads to an uneven wall.

I have researched *polytype* semiconductor heterostructures. A material can exist in different crystal structures (different stacking of atoms). Polytype heterostructures are heterostructures made with the same semiconductor material, but different crystal structure. To refer back to the wall example, polytype heterostructures would be like using the same bricks but laying them on top of each other slightly differently, as shown in figure 3. Because of the difference in stacking, the different crystal structures of the same semiconductor material

have different bandgaps and energy bands, despite using the same atoms. It is possible to use only a single material to make heterostructures with different bandgaps, while the interfaces are still entirely smooth without strain or mixing.

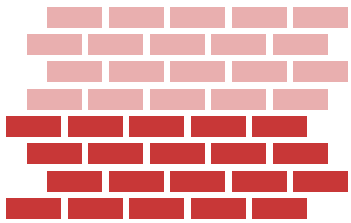

Figure 3: A brick wall where all bricks are the same size but only the stacking order changes. Here the interface is sharp and even.

In my thesis I look at different types of polytype semiconductor heterostructures for different nanoscale applications. Firstly, because nanoscale applications are very small, they have a lot of surface area for very little actual material. Therefore I have looked at the influence of the semiconductor-air interface on the semiconductor properties. I found that this influence is rather large, especially on measurements of the bandgap difference between the two crystal structures. Since all the measurements of polytype heterostructures are done in so called nanowires: small rods of semiconductor material about 100 nm wide (1000 times thinner than a hair), the effect of the semiconductor-air interface should be taken into account whenever bandgap measurements are attempted.

Secondly I looked at the possibility of using polytype heterostructures instead of heterostructures of different materials for high speed electronic components, since the ideal interface could lend itself to even faster semiconductor transistors. In high speed electronics, electrons that carry the current through the semiconductor travel at high speed, often in a very narrow channel of a few nanometers wide. If the walls of this channel are made using material heterostructures, the electrons can bounce against the roughness of the walls, slowing down in the process. In polytype heterostructures that would be less of an issue. I have shown that it is indeed possible to create a polytype heterostructure that could be used as a transistor.

Lastly I looked at really small polytype semiconductor structures called quantum dots. These heterostructures are of the order of 10 nm in each direction, making them 100 billion times smaller in volume than a grain of sand. At this small size the behavior of the electrons is strongly influenced by quantum mechanics. Since the interface of a heterostructure with different materials is not smooth or uniform, the electronic properties of material quantum dots are hard to predict. I have shown that it is possible to create polytype quantum dots with well defined dimensions. I also show that therefore it is possible to predict the electronic properties of these polytype quantum dots before creation. This is crucial for the design of possible applications.

List of papers

Publications included in the thesis

I. **Radial band bending at wurtzite–zinc-blende–GaAs interfaces**
Geijselaers, I., Lehmann, S., Dick, K.A. and Pistol, M.-E.
Nano Futures, Vol. 2, No. 3, p. 035002, 2018.
I performed the optical measurements, data analysis and calculations, and took the leading role in the preparation of the manuscript.

II. **Two-dimensional electron gas at wurtzite–zinc-blende InP interfaces induced by modulation doping**
Geijselaers, I., Lehmann, S., Dick, K.A. and Pistol, M.-E.
Applied Physics Letters, Vol. 116, No. 23, p. 232103, 2020.
I took part in project planning, performed the optical measurements and data analysis, and took the leading role in the preparation of the manuscript.

III. **Atomically sharp, crystal phase defined GaAs quantum dots**
Geijselaers, I., Vainorius, N., Lehmann, S., Pryor, C.E., Dick, K.A. and Pistol, M.-E.
Manuscript
I was in charge of project planning, performed the optical measurements, data analysis and calculations, and took the leading role in the preparation of the manuscript.

Other publications beyond the scope of this thesis

IV. **Band bending at the heterointerface of GaAs/InAs core/shell nanowires monitored by synchrotron X-ray photoelectron spectroscopy**
Khanbabaee, B., Bussone, G., Knutsson, J.V., Geijselaers, I., Pryor, C.E., Rieger, T., Demarina, N., Grützmacher, D., Lepsa, M.I., Timm, R. and Pietsch, U.
Journal of Applied Physics, Vol. 120, No. 3, p. 145703, 2016.

V. **Intersubband Quantum Disc-in-Nanowire Photodetectors with Normal-Incidence Response in the Long-Wavelength Infrared**
Karimi, M., Heurlin, M., Limpert, S., Jain, V., Zeng, X., Geijselaers, I., Nowzari, A., Fu, Y., Samuelson, L., Linke, H., Borgström, M.T. and Pettersson, H.
Nano Letters, Vol. 18, No. 1, p. 365-372, 2018.

VI. **N-type doping and morphology of GaAs nanowires in Aerotaxy**
Metaferia, W., Sivakumar, S., Persson, A.R., Geijselaers, I., Wallenberg, L.R., Deppert, K., Samuelson, L. and Magnusson, M.H.
Nanotechnology, Vol. 29, No. 28, p. 285601, 2018.

VII. **Template-assisted vapour–liquid–solid growth of InP nanowires on (001) InP and Si substrates**
Jam, R.J., Persson, A.R., Barrigón, E., Heurlin, M., Geijselaers, I., Gómez, V.J., Hultin, O., Samuelson, L., Borgström, M.T. and Pettersson, H.
Nanoscale, Vol. 12, Issue 2, p. 888-894, 2020.

Acknowledgements

Throughout my time at Lund university I have had the pleasure of meeting and working with many incredible people. The fun and open environment at FTF has given me countless great memories. It will be impossible to thank everyone that helped me in the last few years, but I will give it a shot.

I want to start by thanking my supervisor Mats-Erik Pistol. You have always approached me and my work with enthusiasm, and that enthusiasm definitely rubbed off on me. You were always very involved with my project, even coming into the lab multiple times a day if I was measuring something potentially interesting. Your knowledge about the subject has always impressed me and I am very happy to have had you as my supervisor.

I also want to thank my co-supervisors, Sebastian Lehmann and Craig Pryor. Sebastian, I can not express how much your kindness and advice has helped me. Your patience and willingness to brainstorm when the measurements were not going smoothly is deeply appreciated. Craig, you have always been very helpful in answering all the questions I had about the calculations. Thank you for all your help.

This work would not have been anywhere near it's current state without the wonderful people who shared the lab with me. Neimantas, you taught me everything I know. I can't emphasize enough how grateful I am with all the help when something in the PL setup inevitably messed up and I got another error that we had never seen before. You made me feel welcome at FTF when I first started my masters all those years ago, and your kindness never stopped. From the bottom of my heart, thank you! Asmita, you still have some time ahead of you in the lab, but I am sure that you too will befriend the lab troll and find your way around the setup. Good luck on the rest of your studies! I also want to thank Simon K., Marcelo, Niklas, Yang Chen and all the others who shared the lab and/or optics group with me.

I also greatly appreciate the help I got from all of the FTF staff who are the main people who make this place work. Special thanks to Alfons, Anastasiia, Anders, Bengt, David F., George, Håkan, Janne, Marica, Sara A. and Johanna Ä.H. for all the help they provided.

My time at FTF has allowed me to get to know so many incredible people. Jonatan, Sven, Lukas, Oskar, David A. and David (D-Dog) B., you all really cheer up my days at the office! Thank you for all the amazing memories. Neimantas, Asmita, Artis, Regina, Damiano, Kushagr, Simon W., Harald, Julia, Karolis, Kristi, Annti, Athanasios, Sara, Sudhakar, Florinda, Hossein, Frida, Marcus, Erik, Martin J., Calle, Laura, Adam, Bengt, Jason, Martin H., Alex, Philip, and everyone else who danced with me, played boardgames with me, played innebandy with me, or just talked to me during lunch, you all made my time here so incredibly much more enjoyable. Thank you.

Special thanks to Oskar for being the best office mate. Sadly, during the Covid time we haven't been able to see each other as much, but I always enjoyed our conversations, the tea breaks and your deep existential questions that came out of nowhere. I wish you all the best with finishing your thesis!

I can not leave all my friends outside of work unacknowledged. Johanna F.J., Despite moving to the other side of the country you have remained one of my most treasured friends. Thank you for all the fun we have together. David (Däjv) B., Stephanie, Martin, Pernilla and Niklas, although most of our adventures were imaginary, they felt real to me. May the dice gods bless you with many nat 20s. Jill, Henrik, Jacob and David (Däjv) B., I can not wish for better friends than you. You helped me through some of the most difficult times in my PhD and I can't thank you enough for that. You made me feel welcome when I first came here and you made it feel like home all these years since. It is such a shame that you are all nerds.

I can not forget everyone in the Netherlands who remained my close friends despite the distance. Frederike, Marion, Olaf, Jeremy, Daan, Hanne, Judith, Annelies, Jille and all of #RU, thank you for sticking with me, even though I so rudely decided to move all the way to Sweden.

I would like to thank my family in the Netherlands, who have been with me through everything. Your support has been invaluable, and, although I don't get to see you quite as much as I would like, you are always with me. Thank you.

Lastly, thank you Casimir. You are the main reason I did not go insane. You are always there for me and I can not be more grateful. Thank you.

Abbreviations and symbols

2DEG	Two dimensional electron gas
a	Lattice constant
a_c	Conduction band deformation potential
$Al_xGa_{1-x}As$	Aluminium gallium arsinide
AlAs	Aluminium arsinide
CCD	charge coupled device
ccp	Cubic close packed
CW	Continuous wave
DOS	Density of states
D_s	Surface state density
E_a	Acceptor level
E_c	Conduction band energy
E_d	Doping level
E_F	Fermi-level
E_g	Bandgap energy
E_{hp}	High EPD emission energy
E_i	Intrinsic energy level
EM	Electron microscopy
EPD	Excitation power density
$E_{type-II}$	Type-II transition energy
E_v	Valence band energy
fcc	Face centered cubic
GaAs	Gallium arsenide
hcp	Hexagonal close packed
HEMT	High electron mobility transistor
InP	Indium phosphide
LED	Light emitting diode
m_0	Electron mass
m_e	Effective electron mass

m_{hh}	Effective heavy hole mass
MOVPE	Metalorganic vapor-phase epitaxy
N_a	p-type doping concentration
NA	Numerical aperture
PL	Photoluminescence
PLE	Photoluminescence excitation
q	Charge
Q_b	Bulk charge
Q_s	Surface charge
Q-dot	Quantum dot
Q-well	Quantum well
Q-wire	Quantum wire
R	Nanowire radius
S	Sulphur
SEM	Scanning electron microscopy
Si	Silicon
SiN	Silicon nitride
STEM	Scanning transmission electron microscopy
TEM	Transmission electron microscopy
Ti:Sa	Titanium sapphire
VLS	Vapor-liquid-solid
V_p	Electrostatic potential
w	Depletion region
wz	Wurtzite
zb	Zinc-blende
ΔE_c	Conduction band offset
ΔE_g	Bandgap energy difference
ΔE_v	Valence band offset
Δ	Observed band offset
λ	Wavelength
$\phi(\mathbf{r})$	Wavefunction
ψ_{Bi}	Built-in potential
ψ_{CNL}	Charge neutral level
ψ_0	Bulk potential
ψ_s	Surface potential
ρ	Density
σ	Hydrostatic strain
σ_{ij}	Strain tensor

Chapter 1

Introduction

Many of todays technological advancements are made possible by semiconductors. They play a key part in many solar cells[1], light emitting diodes (LEDs)[2] and transistors[3,4], and also provide a great platform for the study of physical principles such as quantum mechanics[5,6]. The most commonly used semiconductor material is silicon, since its abundance and easy purification[7] allow for low cost production of electronic components. Silicon, however is not ideal for all applications. LEDs, for example require optically active semiconductor materials, while silicon has little to no light emitting capabilities[8]. LEDs are instead often made of so-called III-V semiconductors[2]: semiconductors that consist of a combination of equal parts chemical elements from the group III and the group V in the periodic table of elements. Examples of this type of semiconductor are Gallium Arsenide (GaAs) and Indium Phosphide (InP), but many more combinations exist, all with different material properties.

The most important feature of semiconductors is the bandgap[8]: a range of energy in which no energy states are located. Electrons can be raised over the bandgap energy (E_g) from the so called valence band energy (E_v) to the conduction band energy (E_c) by thermal energy or photons, leaving behind a hole in the valence band. When an electron is positioned in the conduction band, it can move freely and the semiconductor can then conduct current[9].

The reason semiconductors are so commonly used is because we can very carefully control their properties. It is, for example, possible to increase the number of electrons in the conduction band by doping the semiconductors: replacing some of the chemical elements with others that can release an extra electron[10]. This allows us to carefully tune the number of electrons in the semiconductor,

which is useful in electrical components like transistors. We can also combine semiconductors with different bandgaps in so called heterostructures or mix semiconductor materials to tune the width of the bandgap[8].

Many semiconductors are crystalline, which means that the atoms in the material are ordered in a three dimensional lattice that repeats in each direction. Most non-nitride III-V semiconductors have the zinc-blende (zb) crystal structure[11]. This is a cubic crystal structure that repeats itself every third layer along a certain crystallographic direction [111]: ABCABCABC.... In some nano structures it is possible to create these semiconductors in another crystal structure, which is not commonly found in the bulk form. In nanowires, rods of material that are only approximately 100 nm in diameter, but can be up to a few μm long, III-V semiconductors can be found in the wurtzite (wz) crystal structure[12,13]. Wurtzite is an hexagonal crystal structure that repeats every second layer: ABABAB..., which causes the material to have different material properties than the zb form, even though they contain the exact same chemical elements in the same amounts[14].

It has only recently become possible to make these wz crystal phase nanowires in a controlled way[15,16]. The controlled crystal phase switching has opened up the possibilities of wz-zb heterostructures of the same material, so called crystal phase or polytype heterostructures[17]. These polytype heterostructures have some advantages over conventional material heterostructures that are made using different materials. The interfaces in polytype heterostructures are atomically sharp over large areas[18], whereas material interfaces tend to exhibit atom intermixing, causing interface roughness[11]. Additionally, depending on the materials used, material interfaces can be strained, which changes the local band structure[11]. But, because the polytype interfaces are made from the same chemical elements, there is minimal strain in the crystal structure[19].

Wurtzite crystal phase nanowires and wz-zb crystal phase heterostructures have both been investigated using many different techniques for many different applications[17,20–25]. A common technique for characterization of optical properties is photoluminescence (PL) spectroscopy[9]. The principle of PL is based on the absorption of photons, which excites electrons from the valence band to the conduction band. When the electron recombines with the hole in the valence band, it emits a photon with the energy of the bandgap. This is a powerful technique that can be used to investigate the band structure properties of different materials or heterostructures[9].

Using PL, and the related photoluminescence excitation (PLE) spectroscopy technique[9], many basic properties of wz III-V semiconductors have been meas-

ured, such as the bandgap[17,26–28], the effective masses[21,29–32], and the valence band offset (ΔE_v)[29,33].

This thesis aims to deepen the understanding of these wz-zb heterostructures and explore possible applications. This is done through PL and PLE spectroscopy on individual nanowires, the result of which has been correlated to electron microscopy studies on the identical nanowires. This combination of characterisation methods is crucial to relate the optical results to the geometry and crystal phase purity of the nanowire samples. The electron microscopy also allows the determination of the dimensions of the heterostructures, which have been used in numerical calculations of the nanowire properties.

This work is described in three papers on wz-zb III-V semiconductor heterostructures. First, I look into the effect of the semiconductor-air surface on the emission from a wz-zb GaAs interface. In a previous study[29] it was shown that the emission from wz-zb GaAs heterostructures was dependent on the diameter of the nanowire. This indicates the presence of so called Fermi-level pinning at the GaAs-air surface. In paper I is shown that there is indeed a diameter dependence which is in line with the expected radial band bending due to Fermi-level pinning. I combine the PL results with an analytical model for Fermi-level pinning and extract the unintentional doping concentration and valence band offset for the wz-zb GaAs interface.

In the second work modulation doped wz-zb InP interfaces are studied. I show that, by doping the wz-InP, a two dimensional electron gas (2DEG) forms on the zb-InP side of the polytype interface. I show that the state filling in the zb-InP affects the PL emission from the zb-wz interface and I give a rough estimate of the valence band offset for the wz-zb InP interface. This work lays the foundation for the exploration of 2DEGs at roughness free interfaces.

Lastly, in paper III I investigate zero dimensional crystal phase quantum dots (Q-dots). The PL and PLE show that multiple energy levels exist in a zb-GaAs Q-dot in a thin (<20 nm) wz-GaAs nanowire. The work also shows that there are Q-dot like states at a single wz-zb GaAs interface in thin nanowires. The PL and PLE results are combined with numerical calculations of the energy levels in the Q-dots. This work shows the potential of crystal phase Q-dots for optical applications.

This thesis is written as an introduction to the three papers included in the work. I will start by giving an introduction to the theoretical concepts in chapter 2. Chapter 3 will cover the experimental methods used in the work. In chapter 4 I will delve into my findings of the three included papers and lastly, in chapter 5, I will offer some concluding remarks and give an outlook on my work.

Chapter 2

Background

In this chapter I will explain some of the physics concepts that are used in this thesis. These concepts include crystal structures and polytypism in semiconductor nanowires. I will also give an overview of semiconductor physics, which includes quantum mechanics and light matter interaction. Lastly I will give an overview of Fermi-level pinning in semiconductor nanowires.

2.1 Polytypism

Many common materials, including most semiconductors, are crystalline: the atoms are ordered and repeated in all three dimensions. The most simple crystal structure is the primitive cubic crystal structure as shown in figure 2.1. The individual atoms lie on the corners of a cube with equal side lengths. This cube is called the unit cell, which is repeated in all directions, and the size of the unit cell is determined by the lattice constants, which in this case are $a = b = c$ and the angle between the vectors is $90°$.[11]

Within a crystal it is possible to identify planes of atoms that are equally spaced. The directions in which these lattice planes repeat are indicated with Weiss indices. These are constructed from the point of interception on the crystal axes. For example: the x direction is the [100] direction, while the z direction is the [001] direction. In terms of planes, in the primitive cubic crystal structure in figure 2.1, the plane created by the lattice vectors b and c is called the (100) plane, since it is repeated in the x (or [100]) direction. Besides these directions, one can also identify repeating planes at different angles, such as the [111] direction, creating all permutations of the basis vectors.[11]

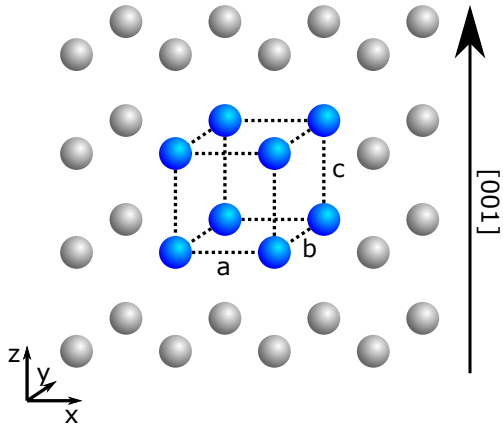

Figure 2.1: An example of a simple cubic crystal structures. The unit cell is indicated in blue with lattice constants $a = b = c$

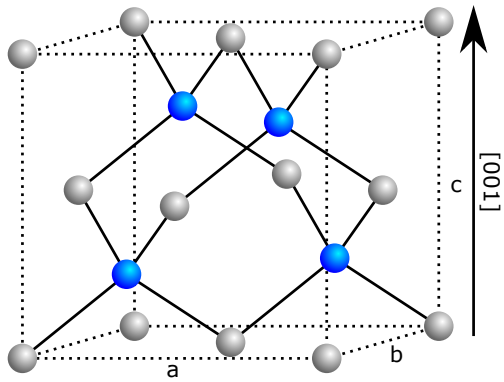

Figure 2.2: The zinc-blende crystal unit cell.

While the example above is very simple, often the crystal structure of materials can take on more complicated forms. Figure 2.2 shows the zinc-blende (zb) crystal structure[19]: a combination of two so called face centered cubic (fcc) crystal structures, one of which is translated by 1/4th in all directions. Here the unit cell consist of multiple atoms of different types, but it is still possible to construct a unit cell that is cubic with the lattice constants $a = b = c$ and corners of 90°. fcc-like crystal structures, such as zb are often called cubic close packed (ccp) as it is one of the most optimal stacking sequences in terms of the fill factor. Assuming the atoms at the crystal sites are hard spheres that border each other, the fill factor, or atomic packing factor, is the fraction of the total

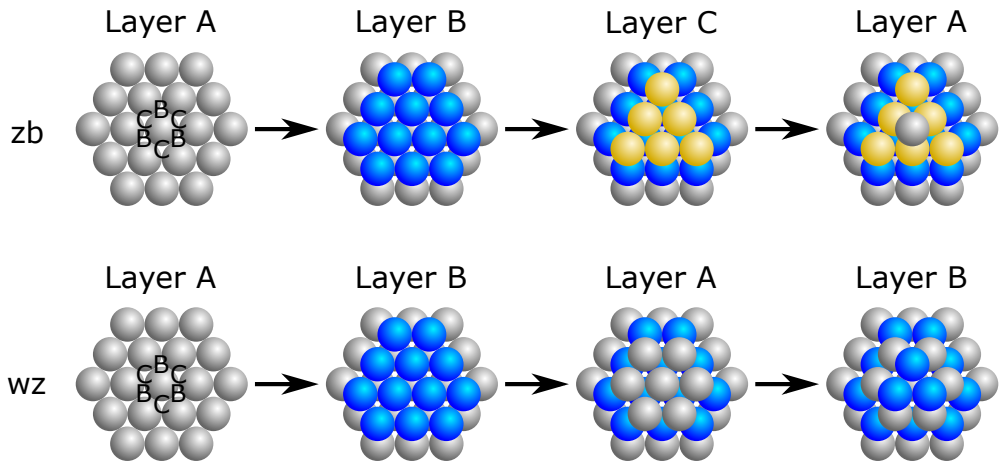

Figure 2.3: The wurtzite and zinc-blende crystal structure in the [0001] and [111] direction, respectively. zb has the ABCABC layer ordering (gray, blue and yellow, respectively). wz has the ABABAB layer ordering (gray and blue, respectively). Each sphere corresponds to two atom sites.

volume that is then occupied by the spheres. In the fcc crystal structure this is as high as 0.74. For comparison, the simple cubic crystal structure has a fill factor of 0.52[11].

In order to better visualize the stacking of the zb and fcc crystal structure, figure 2.3 shows the crystal structure along the [111] direction. Here sets of two atoms are approximated with hard spheres. When the first layer (layer A) of spheres is closely packed it will show a hexagonal packing. The closest possible packing of the second layer would be in one of the valleys between 3 of those balls, such as layer B. On top of layer B there can be two different approaches: back on top of the previous layer A, or a new layer C. In the latter case this would give the ccp zb crystal structure with stacking order ABCABCABC.

If instead the third layer has the positions directly on top of layer A, such as in figure 2.3 a different crystal structure is formed: the hexagonal close packed (hcc) wurtzite (wz) crystal stucture[19]. This crystal structure is shown in figure 2.4. Where the zb crystal structure is cubic, the wz crystal structure is hexagonal, which means that the angle between the lattice vectors a and b is 120° and $a = b \neq c$[11].

Many non-nitride III-V semiconductors, including InP and GaAs, are commonly found in the zb crystal structure[34]. Recently, however, scientists have been able to create a number of III-V semiconductors, again including InP and GaAs, in

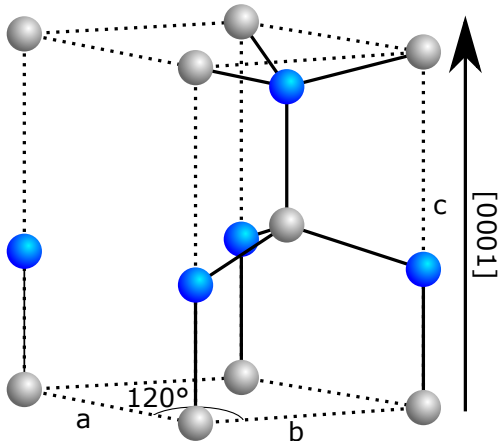

Figure 2.4: The wurtzite crystal structure unit cell.

the wz crystal structure in a controlled manner[15]. To achieve this, the semiconductors are grown into nanowires: semiconductor rods with a high aspect ratio. By changing the conditions during growth, it is possible to switch between zb and wz crystal structure, creating so called polytype heterostructures, while retaining the same binary compound[16].

In many applications it is necessary to use a combination of semiconductor materials, since different semiconductor materials have different electronic and optical properties. When one crystalline semiconductor is created on top of another crystaline semiconductor, they form a heterostructure. At the interface between these different materials a few phenomena can occur, two of which are illustrated in figure 2.5[11]. Since different semiconductors have different lattice constants, strain and even stacking faults, can occur at the interface. In addition, when the heterostructures are created, the switching between the two materials is not instantaneous, causing atom intermixing. Both lead to interface roughness, which can be undesirable for applications where fast electron or hole gasses or well defined quantum structures are used.

Polytype heterostructures are created using different crystal structures of the same material rather than using different materials. This has a few advantages over conventional material heterostructures. Since the material on either side of the interface is the same with just a different stacking order, the interatomic distances are very similar. Therefore there is little to no strain[35]. For the same reason, polytype heterostructures also exhibit no atom intermixing[19], creating perfectly smooth and well defined interfaces.

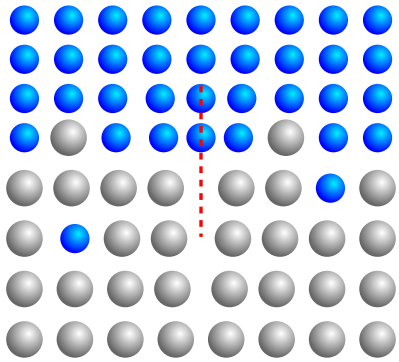

Figure 2.5: A schematic representation of strain and intermixing at a material interface. The red line indicates a stacking fault due to the difference in lattice constant between the gray and blue crystal.

2.2 Semiconductor physics

2.2.1 Electronic band structure (and heterostructures)

As mentioned in chapter 1, the most important property of semiconductors is the bandgap. To understand where the concept of the bandgap originates from, we should look at the movement of electrons through different materials[36]. Electrons in free space do not have any external potential that can affect their movement. They move through free space like waves of the form $\phi(\mathbf{r}) = \exp(\pm \mathrm{i}\mathbf{k} \cdot \mathbf{r})$, where $\mathbf{k}$ is the wavenumber of the electron wave, which is related to its wavelength (λ) through $|\mathbf{k}| = k = \frac{2\pi}{\lambda}$.

An electron can have a wavefunction that consists of two or more of these free electron wavefunctions. Such a combination is called a superposition and can be written in the form of $\phi(x) = A\exp(\mathrm{i}kx) + B\exp(-\mathrm{i}kx)$ where A and B are normalization constants. For simplicity only one dimension is considered. In this specific example the electron has a wavefunction of the form $\phi(x) = A\sin(kx) + B\cos(kx)$, whose electron densities $\rho(x) = |\phi(x)|^2$ are sinusoidal, with a spatial phase shift. In free space there is no potential the electrons interact with, but when an electron travels through a semiconductor, it encounters the periodic atomic potential of the crystal lattice. For electrons with a wavelength of exactly the lattice constant, the electron densities can either be at the low potential position or at the high potential position, as shown in figure 2.6. This means that although two waves have the same wavenumber, they have a different energy. This energy difference is the bandgap (E_g) of the semiconductor, and no energy eigenstates can exist within that bandgap.[36]

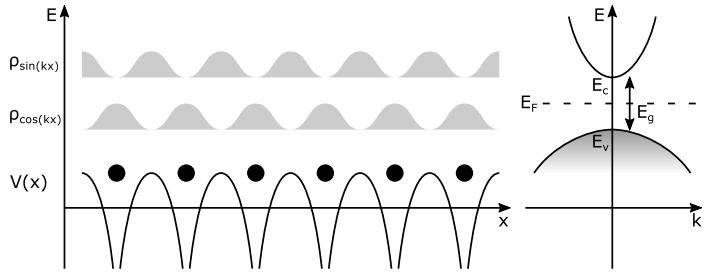

Figure 2.6: The creation of a bandgap due to the density profile of the electron wave functions interacting with the atomic potential of the lattice. The atoms are indicated by the black circles, the atomic potential is in black and the electron densities of both the cosine and the sine are indicated in gray. To the right a schematic representation of the band structure is shown.

The shape and position of the electron bands below and above the bandgap (the valence and conduction bands respectively, indicated with E_v and E_c in figure 2.6), are important properties of semiconductors. As electrons are fermions they adhere to the Pauli-principle: no two electrons can occupy the same state. This means that if we look at the states in the electronic bands of a semiconductor, the electrons fill the states successively until all states in a band are filled, after which they start occupying the next band. The energy level where only half the states are filled is called the Fermi-level (E_F), and for semiconductors, this energy level is inside the bandgap (as shown in figure 2.6).[36]

When an electronic band is completely filled with electrons, like the valence band in figure 2.6, the electrons can not carry any current, as there are no free states available for an electron to move into. However, when an electron is excited from the valence band into the conduction band, for example by absorbing a photon, the electron can move freely in any direction. The empty state the electron leaves behind can be described as a hole: a quasi-particle that behaves like an electron, but with opposite wavenumber and charge. These holes carry current in the same way electrons do, but often are characterized by different masses, as they interact differently with the periodic potential of the crystal.[36]

As pointed out in chapter 1 it is possible to modulate the number of holes and electrons in a semiconductor by replacing one of the chemical elements with an element with more or fewer electrons. These, so called, doping atoms create energy states in the bandgap, that are usually close to the valence band for acceptors or close to the conduction band if the doping atoms are donors. An acceptor receives an electron from the valence band when it is ionized, leaving behind a hole, while an ionized donor adds an electron to the conduction band. The ionization energy, the energy difference between the valence band and the

acceptor level E_a, or the doping level and the conduction band E_d, is small compared to E_g. A material of this kind is considered p-type or n-type doped, respectively.[8]

It is important to realize that, although doping can be done with intent, there can also be doping atoms incorporated unintentionally when the semiconductor material is created. For example, GaAs nanowires grown with a technique called metalorganic vapor-phase epitaxy (MOVPE) can have incorporation of carbon during growth. This can be n-type or p-type doping, depending on the growth conditions[11]. For MOVPE grown InP nanowires, it is common to have phosphorus vacancies that function as shallow donors[37,38]. In both unintentionally doped GaAs and InP, other doping atoms can be used to counter-dope the nanowires, for example, with iron in the case of InP, and make them semi-insulating[39].

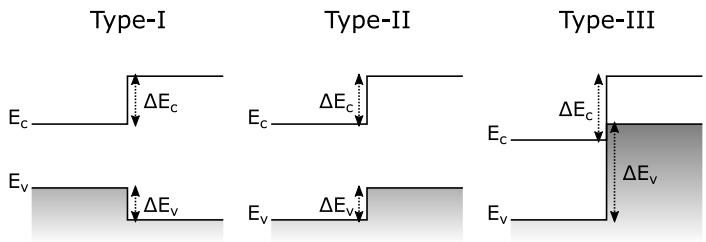

Figure 2.7: Examples of a type-I (straddling), type-II (staggered) and type-III (broken-gap) alignment.

As already mentioned, different materials have different bandgaps. This creates three possible ways the bands can be aligned, displayed in figure 2.7[40]. A type-I band alignment happens at an interface between a small bandgap and a large bandgap material. This type is also called a straddling band alignment, as both the holes and electrons encounter a positive step at the interface of size ΔE_v and ΔE_c. Charge carriers generated in the large bandgap material will accumulate in the small bandgap material before recombining. The second type is called a type-II or staggered band alignment. In this case electrons in the conduction band still encounter a positive step ΔE_c, but the holes in the valence band encounter a negative step ΔE_v. This means the electrons and holes will gather in the different materials and an electric field will form across the interface. The final type of band alignment is a type-III or broken-gap alignment. Here the valence band of one material overlaps with the conduction band of the other material. This results in a free exchange of holes and electrons between the two materials until the movement of charge carriers is halted by the electric field

generated by the charge difference[36]. Currently, all III-V semiconductor wz-zb polytype heterostructures mentioned in chapter 1 are assumed to have type-II band alignment[14,34,41].

2.2.2 Quantum confinement (and DOS)

As described above, free electrons behave like plane waves with a wavefunction $\phi(\mathbf{r}) = \exp(\pm i\mathbf{k} \cdot \mathbf{r})$. The wavenumber $\mathbf{k}$ of the electron is dependent on the energy E through the time independent Schrödinger equation[42]:

$$\hat{H}\phi(\mathbf{r}) = -\frac{\hbar^2}{2m}\nabla^2\phi(\mathbf{r}) + V(\mathbf{r})\phi(\mathbf{r}) = E\phi(\mathbf{r}) \tag{2.1}$$

Here $\hat{H}$ is the Hamiltonian operator, $\hbar$ is the reduced Planck constant with a value of $1.05457 \cdot 10^{-34}$ Js, m is the mass of the electron and $V(\mathbf{r})$ is the spatially dependent potential. In free space $V(\mathbf{r})$ is constant and can be set to 0, but in semiconductor heterostructures the potential landscape is dependent on the conduction bands of the materials involved.

When the potential landscape contains small features, the wavefunction of an electron will be squeezed and the energy of the electron becomes quantized. This phenomenon is called confinement and the quantized energy levels can be calculated by solving the Schrödinger equation. An example of this behavior is the finite square well, a one-dimensonal version of which is shown in figure 2.8. Here a material with a low lying conduction band (material B) is surrounded by materials with a high lying conduction band (material A). An electron existing in material B will experience a potential step in either direction, resulting in it being trapped in the well. Because of this constraint the wavefunction of the electron in material B will not be a free wave, but rather a standing wave with a wavefunction $\phi(x) = A\sin(kx)$ or $\phi(x) = B\cos(kx)$[36].

The electron trapped in the well will not have enough energy to overcome the barrier of material A. In classical physics that would mean that there is no chance for the electron to exist in material A. However, in quantum mechanics, there is a phenomenon called tunneling: the wavefunction of an electron is able to penetrate a potential barrier, exponentially decreasing in amplitude. Since the total wavefunction needs to adhere to the Schrödinger equation the wavefunction in material A and material B need to match. This means that both the wavefunction and its derivative need to be continuous. There is a limited number of k for which this is true, which means that the energies the electrons can have are also limited to specific levels[36].

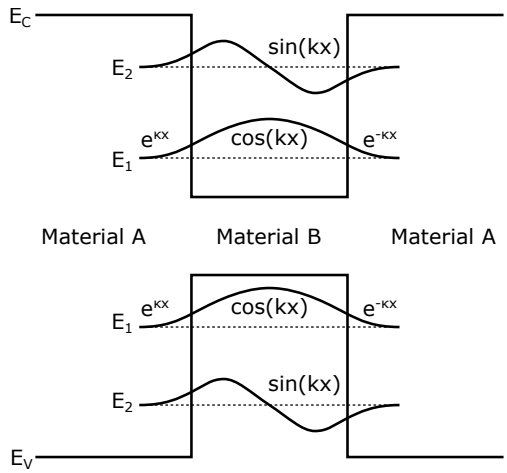

Figure 2.8: Confinement of electrons and holes in a one-dimensional Q-well. In the well (material B) the wavefunctions of the electrons and holes are described by sinus and cosinus functions, while in the barrier (material A) the wavefunctions are described by decaying exponentials.

In the valence band the holes behave similar to electrons. Therefore when a material with a low lying valence band (material A) surrounds a material with a high lying valence band (material B) similar energy states will occur (see figure 2.8), occupied by holes rather than electrons.

Figure 2.8 shows confinement in one dimension, but it is possible to have confinement in all three dimensions. Two dimensional heterostructures are called quantum wells (Q-wells), one dimensional heterostructures are quantum wires (Q-wires) and zero dimensional heterostructures are quantum dots (Q-dots).

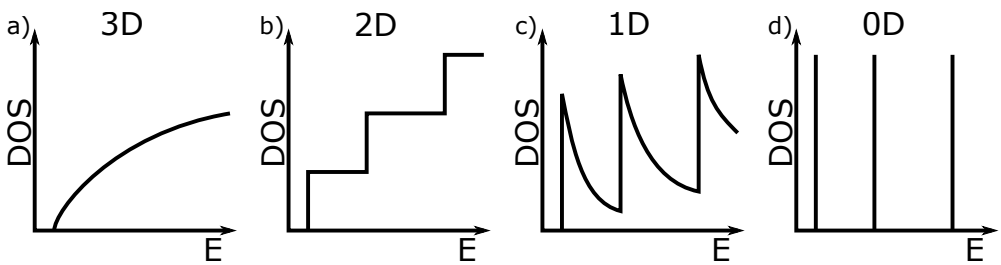

Figure 2.9: The density of states for a) a 3D bulk system, b) a 2D Q-well system, c) a 1D Q-wire system and d) a 0D Q-dot system.

The density of states (DOS) is the number of states available for an electron to exist in[36]. This DOS is dependent on the energy of the electron. For a bulk

material, the density of states increases with increasing energy with a square root dependency ($\rho_{3D} \propto \sqrt{E}$), as shown in figure 2.9a. Because of the quantum confinement, the number of states available for the electron changes, therefore the density of states changes. Figure 2.9b, c and d show the DOS for a 2D, 1D and 0D system. They are $DOS_{2D} \propto const$ for a Q-well, $DOS_{1D} \propto \frac{1}{\sqrt{E}}$ for a Q-wire and $DOS_{0D} \propto \delta(E)$ for a Q-dot.

2.2.3 Charge carrier generation and recombination

The process of PL is schematically explained in figure 2.10. A photon with energy $\hbar\omega_{in} > E_g$ can excite an electron from the valence band to the conduction band. From there it loses its excess energy in the form of phonons to the crystal lattice and relaxes down to the conduction band edge. The hole in the valence band relaxes up to the valence band edge from where the hole and electron can recombine sending out a photon. There are a number of different processes that can occur. The most common process is the recombination over the bandgap, sending out a photon with energy $\hbar\omega_{out} = E_g$. In a very clean material, it is even possible for the electron to bind to the hole as if it was an atom. This is called an exciton and it decreases the energy emitted on recombination by the exciton binding energy[8].

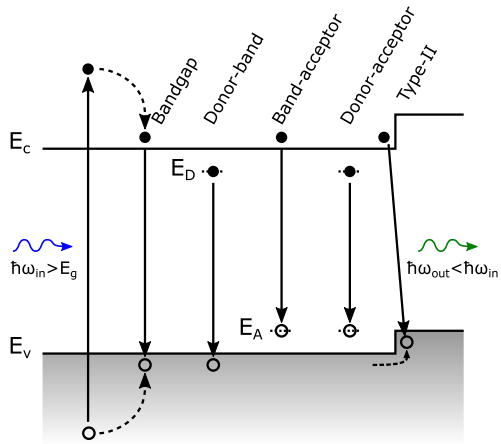

Figure 2.10: The principle of photoluminescence spectroscopy. Light with a energy higher than the band gap excites an electron-hole pair. Recombination is possible from, among others, band edge to band edge, donor level to band edge, band edge to acceptor level, donor to acceptor level and across a type-II interface.

It is also possible for the electron or the hole to relax into the doping impurity level close to the conduction or valence band. From there it can recombine either

from the impurity level to the band edge, from the band edge to the impurity level, or from an impurity level to another impurity level. All three of these recombination processes emit photons with an energy less than the bandgap $\hbar\omega_{out} < Eg$[8].

The final process is that of spatially indirect type-II recombination. As mentioned before in chapter 2.2.1, at type-II interfaces the electrons gather in one material while the holes gather in the other material. Although the electrons and holes are not in the same physical place, it is still possible for them to recombine and emit a photon. The electron and hole wavefunctions extend into their respective barriers, causing them to spatially overlap allowing recombination across the type-II interface[43]. The energy of the emitted photon is lower than the bandgap energy by the valence band offset ($\hbar\omega_{out} = E_g - \Delta E_v$). This makes it possible to determine the valence band offsets of type-II interfaces, such as wz-zb GaAs and InP polytype interfaces.

The recombination across a type-II interface (type-II recombination) is a slow process compared to band to band recombination, with lifetimes up to 10 ns[44]. The process is schematically shown for a wz-zb GaAs interface in figure 2.11. When excited above the bandgap, the electrons will accumulate in the zb-GaAs while the holes accumulate in the wz-GaAs. This spatial separation causes an electric field across the type-II interface, in its turn causing triangular wells to form at either side of the interface[17,43,45]. At high excitation power density (EPD) these triangular wells are completely filled with charge carriers. The higher occupied states have a higher overlap leading to larger recombination efficiency, and thus type-II PL for high EPD will have an energy which is close to the bandgap emission[17,43,45].

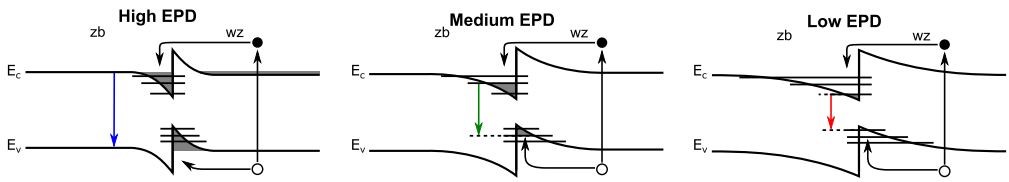

Figure 2.11: The spatially indirect recombination across a wz-zb GaAs interface at high, medium and low EPD.

When the EPD decreases, so will the generation of charge carriers. The charge accumulation on either side of the interface will be less, which has two separate effects. Firstly, the electric field across the type-II interface decreases, which flattens out the triangular wells, reducing the distance between the energy levels in the triangular wells, both for the holes and the electrons. And secondly, fewer charge carriers occupy said energy levels. Combined, these effects lead to

a decrease in energy of the type-II recombination[17,43]. This decrease in type-II PL energy continues until the charge carriers only occupy the lowest level in the triangular wells. At this point the decrease in energy of the type II emission stops. This energy level is referred to as the type-II transition energy ($E_{type-II}$).

Note that even at very low EPD, there is still some band bending at the type-II interface. This is because, even when there is no charge accumulation at the interface, the Fermi-level in the wz semiconductor has to be at the same energy as in the zb, far away from the interface[36]. The Fermi-level of an intrinsic (or unintentionally doped) semiconductor needs to be in the middle of the bandgap (or at the doping level) far away on both sides of the interface. This leads to a small amount of band bending, even if there are no charge carriers generated. Due to this intrinsic band bending, the type-II transition energy can not directly be used to determine the band offset, but instead leads to an "observed band offset" Δ, which can be related to the band offset if the confinement energy of the triangular wells is known.

It is possible for electrons and holes to recombine in so called non-radiative recombination processes, in which the excess energy is released in form of phonons (heat), rather than photons. An example of such a process is Shockley-Read-Hall (or trap-assisted) recombination. In this process an electron and hole recombine via an energy level located in the bandgap, also referred to as a trap level, releasing its energy to the crystal lattice in the form of phonons. These traps are often caused by impurities or crystal defects. Another source of trap states are so called surface states. These states exist due to a number of reasons, like dangling covalent bonds, bonding to other materials or interface traps created by oxidation of the surface[46–48]. The density of these surface states is dependent on the semiconductor material as well as on any possible surface treatment such as passivation of the semiconductor material. In order to reduce the influence of surfaces states it is possible to passivate the surface, for example by covering it with a well controlled oxidation layer or by an epitaxially grown layer of another semiconductor[8].

2.3 Fermi-level pinning

Nanowires are high aspect ratio semiconductor structures with a large surface-to-volume ratio. This means that surface states, as described in section 2.2.3, can greatly influence the optical properties of nanowire semiconductor structures through non-radiative recombination. Surface states can be classified as acceptor states (neutral when empty) and donor states (neutral when filled). In the

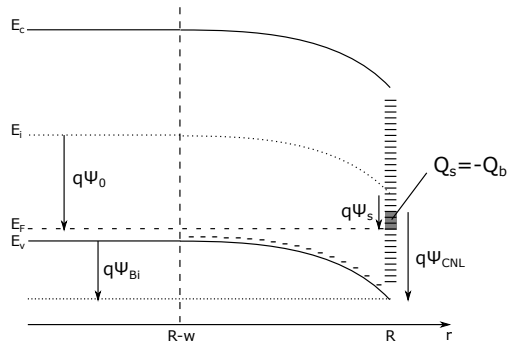

Figure 2.12: A schematic explanation of the mechanism behind band bending at a semiconductor surface due to Fermi-level pinning. The bulk potential is given by ψ_0 which is multiplied with the charge q to convert to energy. The potential at the surface is given by ψ_s. The difference between these quantities is the built-in potential (ψ_{Bi}) The charge neutral level is given by ψ_{CNL}. The charge on the surface (Q_s) is equal but opposite in sign to the charge in the depletion region (Q_b) of width w.

simplyfied model illustrated in figure 2.12, it is possible to define a charge neutral level: the energy above which the surface states are acceptor states and below which the states are donor states. If there is a high density of surface states, the Fermi-level will be pinned close to the charge neutral level[8]. If the semiconductor material is doped, this Fermi-level pinning leads to bending of the bands, as shown in figure 2.12 for a p-type doped semiconductor. The potential at the surface (ψ_s) is smaller than the potential in the bulk semiconductor (ψ_0). A part of the semiconductor is depleted of charge carriers, the so called depletion region (w) which is negatively charged with a charge Q_b because of the ionised acceptors. This charge is countered by the surface charged by ionised surface states $Q_s = -Q_b$. The difference in potential between the bulk semiconductor far from the interface and the potential on the surface of the semiconductor is called the built-in potential $\psi_{Bi} = \psi_0 - \psi_s$. Note that how much ψ_s differs from ψ_{CNL} is dependent on the density of surface states D_s. If D_s is very high, for example for GaAs semiconductor-air interfaces, it is possible to make the approximation that the Fermi-level is pinned exactly at ψ_{CNL}, and thus $\psi_s = \frac{E_i}{q} - \psi_{CNL}$, where q is the electron charge and E_i is the intrinsic energy level, positioned in the middle of the band gap[8,49].

The concept of Fermi-level pinning and surface states becomes important for high surface-to-volume nanostructures, such as nanowires. Especially for lightly doped nanowires, it is possible for the depletion region to be larger than the radius of the nanowire. These nanowires are considered fully depleted, meaning that the ionized region extends throughout the entire nanowire. In figure 2.13

this is shown for a p-type doped GaAs nanowire. In the thin nanowire, the Fermi-level will not be close to the valence band, as would be expected in bulk p-type GaAs, even in the center of the nanowire. In this case, the potential in the center of the nanowire, ψ_0, is smaller than in bulk p-type GaAs. While fully depleted, an increase in nanowire diameter leads to an increase in the radial band bending and thus in ψ_{Bi}. This is illustrated in figure 2.13.

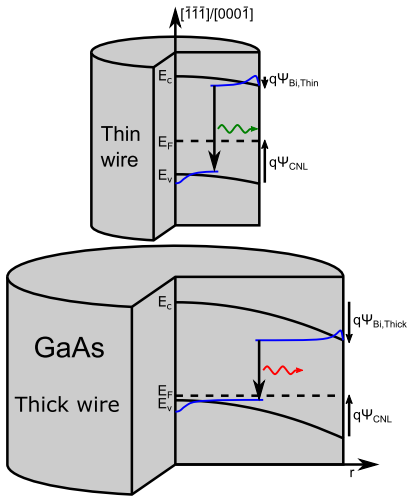

Figure 2.13: A schematic explanation of radial band bending in a GaAs nanowire. The electron and hole wavefunctions are shown in blue. ψ_{Bi} increases with increasing nanowire diameter, leading to a decrease in recombination energy.

As there is band bending in the radial direction, the charge carriers in the valence and conduction band will separate (see figure 2.13). The electrons gather in the conduction band minimum (for a p-type nanowire, at the surface) and the holes gather in the valence band maximum (in case of a p-type nanowire, in the center). By tunneling into the bandgap, it is possible for the charge carriers to recombine and send out a photon, however, the recombination energy is lower than the bandgap energy. This phenomenon is known as the Franz-Keldysh effect [36,50]. The decrease of the emission is exactly $q\psi_{Bi}$, which is dependent on the nanowire radius.

The spatial separation of the charge carriers decreases the overlap between the wavefunctions, which in turn decreases the PL yield [36]. The spatial separation is larger for larger diameter nanowires, so the radial band bending dependent emission for larger diameter nanowires will decrease. This is only relevant for long lifetime charge carriers, like those at a type-II interface. The bandgap

emission is less influenced by the radial band bending, although experiments have reported an influence of nanowire diameter on the low energy tail of the bandgap emission.[50].

2.3.1 Mathematical description

In this section I provide a mathematical basis to calculate the radial band bending in nanowires. For a thorough discussion of the matter, see reference [49]. The description here has been adjusted for GaAs nanowires, which are assumed to have very high D_s and low p-type doping (N_A). The important quantities are defined in figure 2.12 for a nanowire with radius R.

When considering the radial band bending in nanowires, we solve the radial Poisson equation

$$\frac{\mathrm{d}^2\psi}{\mathrm{d}r^2} + \frac{1}{r}\frac{\mathrm{d}\psi}{\mathrm{d}r} = -\frac{\rho}{\varepsilon}, \tag{2.2}$$

where ψ is the electric potential, ρ is the bulk charge density and ε is the permittivity of the material. The general solution to this differential equation is

$$\psi(r) = -\frac{\rho}{4\varepsilon}r^2 + C_1 \ln(r) + C_2 \tag{2.3}$$

with C_1 and C_2 constants that can be found using the boundary conditions. The boundary conditions are different in the case of thick nanowires ($R > w$) and thin, fully depleted nanowires ($R < w$). To determine w however, we need to start with the case $R > w$.

Thick nanowires $R > w$

The boundary conditions are that the potential is the bulk potential outside the depletion region, and that the potenial is continuous at the boundary of the depletion region:

$$\psi(R-w) = \psi_0 \tag{2.4}$$

$$\left.\frac{\mathrm{d}\psi(r)}{\mathrm{d}r}\right|_{r=R-w} = 0. \tag{2.5}$$

Note that these nanowires are lightly p-type doped, and the band bending is considered at low temperatures ($T \approx 7$ K), so the ψ_0 is very close to the impurity level of the acceptor atoms (E_a/q). In the depletion region, all acceptors are ionized, so the charge density is $\rho = -qN_A$.

After solving for the boundary conditions the potential in the nanowire is given by

$$\psi(r) = \frac{qN_A}{4\varepsilon}\left(r^2 - (R-w)^2 - 2(R-w)^2 \ln\left(\frac{r}{R-w}\right)\right) + \psi_0 \tag{2.6}$$

We know that at the surface the potential is ψ_s. We also know that the total surface charge per unit length ($Q_s = 2\pi R q^2 \left(\psi_s + \psi_{CNL} - \frac{E_g}{2q}\right) D_s$) is equal to the charge of the depletion region per unit lenght ($Q_B = -\pi\left((R-w)^2\right) - R^2\right) qN_A$). This means that the depletion region can be found by solving

$$\psi(R) = -\frac{N_A\left((R-w)^2 - R^2\right)}{2qRD_s} + \frac{E_g}{2q} - \psi_{CNL}. \tag{2.7}$$

This can not be solved analytically, and has to be done numerically. Solving equation (2.7) for w shows that the depletion width gets larger for lower doping concentration. This makes sense as the total charge should remain equal. It is clear from equation (2.7) that a high surface state density leads to $\psi_s = \frac{E_i}{q} - \psi_{CNL}$ as mentioned before.

Thin nanowires $R < w$

The nanowires used in this work are lightly doped and are fully depleted. In the case of fully depleted nanowires, the potential in the center of the nanowire does not reach the bulk potential; instead ψ_0 needs to be calculated from the boundary conditions. For a fully depleted nanowire the boundary conditions are given by

$$\psi(0) = \psi_0 \tag{2.8}$$

$$\left.\frac{\mathrm{d}\psi(r)}{\mathrm{d}r}\right|_{r=0} = 0. \tag{2.9}$$

The potential in a fully depleted nanowire has a much simpler form than equation (2.6):

$$\psi(r) = \psi_0 - \frac{qN_A}{4\varepsilon} r^2 \tag{2.10}$$

Using the same technique as above, equating the surface charge and the charge in the depletion region, ψ_s, and thus ψ_0, can be found:

$$\psi(R) = \psi_0 - \frac{qN_A}{4\varepsilon} R^2 = \psi_s = \frac{RN_A}{2qD_s} + \frac{E_g}{2q} - \psi_{CNL}. \tag{2.11}$$

The built-in potential is defined as

$$\psi_{Bi} = \psi_0 - \psi_s = \frac{qN_A}{4\varepsilon} R^2. \tag{2.12}$$

For fully depleted nanowires this quantity is only dependent on the doping concentration N_A and the radius of the nanowire R. This is an important result, as it shows that for sufficiently high surface state density, sufficiently low doping concentrations and sufficiently thin nanowires the surface is irrelevant to ψ_{Bi} and thus the decrease of the PL emission. It also shows clearly that the decrease of PL emission is dependent on the radius of the nanowire. It is important to note that for unintentionally p-type doped nanowires ($N_A \approx 10^{16}$ cm^{-3} [51]) and a typical charge neutral level for GaAs ($\psi_{CNL} = 0.53$ V[49]), nanowires with diameter up to 600 nm are fully depleted.

Chapter 3

Experimental methods

In this chapter the experimental techniques that are used in this work are described. All papers in this thesis involve the manufacturing of nanowires, the optical spectroscopic investigation with techniques such as photoluminescence spectroscopy and photoluminescence excitation spectroscopy, and the structural investigation of the nanowires using both optical and electron microscopy. Besides these techniques this chapter also explains calculation methods used in this work and I will finally go into details about the sample preparation and procedures of my investigations.

3.1 Nanowire growth

A common way to create III-V nanowires is through the so called vapor-liquid-solid (VLS) growth mechanism[12], for example, in a metalorganic vapor-phase epitaxy (MOVPE) system[52]. The process is displayed in figure 3.1. A gold nanoparticle is deposited on a semiconductor substrate. The substrate is heated in a reducing atmosphere to desorb residual oxides from the substrate surface and to melt the gold particle. The III-V precursors are introduced in gas phase. In MOVPE these precursors are often carbon-based groups with metal atoms attached to them, hence the term metalorganic. The precursors decompose and the group-III element alloys with the gold particle, lowering the melting point and forming a liquid alloy droplet. Both group III and group V species are supplied in excess so that the material concentration in the droplet gets supersaturated and precipitation can occur. After nucleation at the VLS triple phase boundary, a layer of semiconductor material is grown underneath the

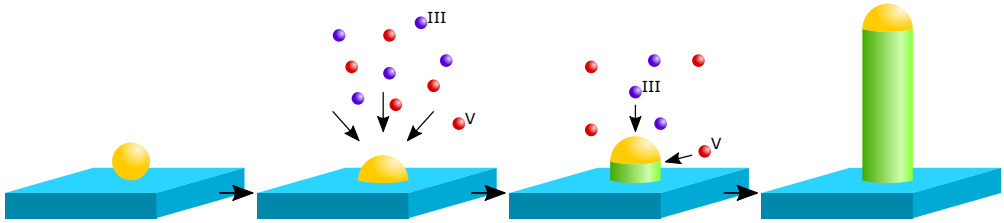

Figure 3.1: A schematic representation of the VLS growth mechanism.

gold droplet and the droplet gets raised from the substrate, balancing on the growing nanowire[52,53]. The size of the gold particle influences the diameter of the resulting nanowire core.

By changing the metalorganic precursors, material heterostructures can be grown. Alternatively, it is possible to grow polytype heterostructures, e.g. by varying the temperature or the group-V precursor molar fraction[15,16]. Doping can be introduced into the nanowire by adding a dopant precursor flow during growth[39]. It is usual to have unintentional carbon incorporation into the nanowire during growth, as the precursors often have carbon based ligands[54].

During nanowire growth it is possible for so called radial overgrowth to occur, which means that the nanowires are not excusively growing in the axial direction directly under the gold particle, but also, or predominantly, in the radial direction. This shell is grown epitaxially: it has the same crystal structure as the core. Such shell growth can occur as a side effect of axial growth. For example, during zb-InP axial growth there is radial overgrowth, both on the zb-InP, as well as on previously grown wz-InP segments. Note that because the overgrowth is along the radial direction, the shell on the wz-InP will still have the wz crystal structure. In some cases a shell is beneficial and grown by design. For example due to surface traps GaAs typically has a low PL yield. In order to passivate the surface states, an aluminium arsinide (AlAs) or an aluminium gallium arsenide ($Al_xGa_{1-x}As$) can be grown. While radial overgrowth is the goal in this case, there is still limited axial growth, creating an axial material heterostructure as well as a radial one.

The nanowires in this work are grown according to the procedures in references [16] and [17]. They are grown in a 3x2" close coupled showerhead and horizontal design MOVPE reactor. The crystal structure of the nanowire is controlled by varying the V-precursor molar fraction[15,16]. A more indepth description of the geometry of the nanowires used in the studies can be found in chapter 4.

3.2 Optical spectroscopy

3.2.1 Photoluminescence spectroscopy

PL spectroscopy is a non-intrusive method for obtaining information about the optical properties of a semiconductor sample[9]. A PL spectrum can give information about quantum confinement, crystal quality, strain and a variety of other properties of the semiconductor sample. PL spectroscopy is a fast technique, which requires a relatively simple optical setup, in its most basic form. This is why it has become a staple in III-V semiconductor physics, both for scientific research and as a technique for rapid feedback[9].

The theory about PL spectroscopy is given section 2.2.3. Charge carriers are excited over the bandgap using a light source with a high photon energy. The charge carriers then release their excess energy and relax to the local minimum. From there they recombine, sending out a photon with the energy of the transition, for example the bandgap energy[9].

The energy of the emitted photons is generally independent of the excitation power or energy, as long as the photon energy is larger than the bandgap. However, at high excitation power density (EPD), it is possible for a shift in emission energy to occur. There are two main effects that can happen. Firstly, at high EPD, the charge carrier generation can exceed the recombination rate at the bandgap edge and cause the energy states above the conduction band and/or below the valence band to fill up until a generation-recombination steady state is reached. This is called state filling and causes the bandgap emission to shift to higher energy[8].

Conversely, if a large amount of generated charge carriers release their excess energy in the form of heat, it is possible to locally heat the semiconductor material. The bandgap energy is inversely proportional to the temperature, therefore, unless the excess heat can easily dissipate, a decrease in bandgap emission energy is observed[9]. This is especially prominent in nanostructures, since they have a relatively low thermal exchange with their environment.

Figure 3.2 shows a schematic drawing of a typical PL setup[9]. The excitation light is generated by a laser with a known wavelength. The laser can be a continuous wave (CW) laser with a fixed wavelength, a CW tunable laser, or a pulsed laser. It is even possible to use a non-coherent light source, like a supercontinuum source, as excitation source. In this work only CW lasers are used. A band pass filter is used to filter the laser light from any unwanted frequencies. If the power source is a tunable power source, a tunable filter is

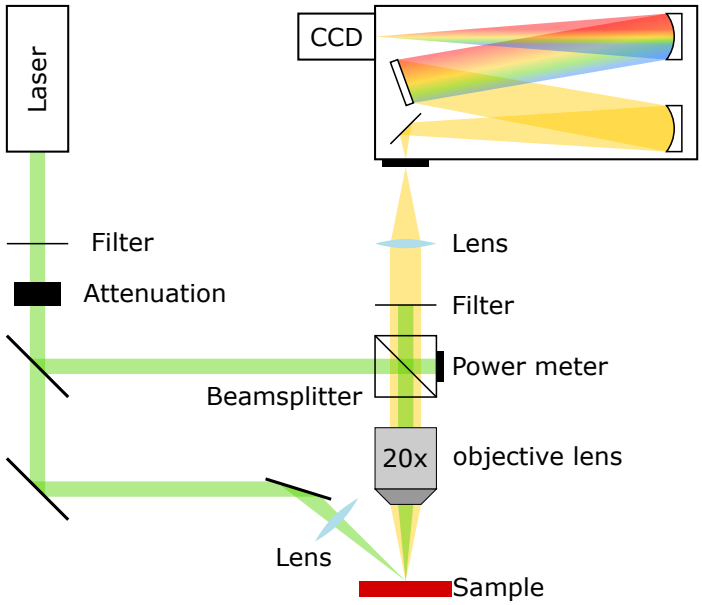

Figure 3.2: A schematic display of a PL setup with side and tight focussing possibilities.

needed. To excite the sample with different EPD, an attenuating element is introduced in the beam. Often this is a filter wheel with different strength neutral density filters, but this can also be done using a fiber attenuator, if fiber optics are used.

The sample can be illuminated in two ways: either focussed through the microscope objective lens using a 50/50 beamsplitter (tight focussing configuration), or from the side at an angle to the sample (side focussing configuration). Although tight focussing configuration gives higher EPD at the sample, it can be beneficial to use side illumination, depending on the sample and the intention of the measurement. Side focussing configuration illuminates a larger area, which is beneficial if the samples are semiconductor nanostructures, like nanowires, as it allows multiple different structures to be characterized at the same time. Tight focussing allows for a spot size limited by the diffraction limit of light. It is possible to do spatially resolved PL using an objective with a resolution of the order of 1 μm. This technique is also called μ-PL. In the work discussed in this thesis, both configurations are used. The work in paper I was done with the 532 nm line of a Nd:YAG laser, in the side focusing configuration. The work in paper II was done using a tunable titanium sapphire (Ti:Sa) laser set to a wavelength of 710 nm, in tight focusing configuration

After illuminating the sample, the PL signal, as well as the scattered laser light, is collected by the objective lens of the microscope. The scattered laser light is filtered using a long pass filter, as the photoluminescence has a lower energy than the laser light (see section 2.2.3). The PL signal is focussed on the entrance slit of the monochromator, where the light gets spectrally resolved using a grating and focussed on a camera. In the work discussed in this thesis, a charge coupled device (CCD) is used. To suppress the thermal noise of the camera, it gets thermoelectrically cooled to approximately -50 °C.

3.2.2 Photoluminescence excitation spectroscopy

In PLE spectroscopy one monitors the PL intensity from a specific transition while exciting the sample at different energies. Typically, a specific transition is chosen as the detection window, for example the groundstate transition in a Q-well, while the excitation energy is scanned from the detection window to higher energies. The technique relies on the fact that the charge carriers that are generated by the excitation laser, lose their excess energy and relax down to the probed transition. The detected PL signal will increase or decrease, depending on the DOS available at the excitation energy[9].

Depending on the detection window, the PLE spectrum will resemble that of absorption measurements, but can be used in circumstances where regular absorption measurements are impossible, for example on individual Q-dots and other individual nanoscale systems. In addition, because the detection window is on one PL active transition, it is possible to distinguish between the DOS from different locations in the same system[9]. For example, if two Q-dots exist in one nanowire, PLE can be used to determine the DOS of either Q-dot, depending on what transition is used as the detection window.

For PLE the same setup is used as shown in figure 3.2. It is however necessary to have a tunable light source, such as a tunable laser or a supercontinuum source. In this work all PLE measurements have been done using a Ti:Sa tunable laser, which is tunable over a wavelength range of 710 nm - 880 nm in tight focusing configuration.

3.3 Microscopy

3.3.1 Optical microscopy

Optical microscopy is a versatile microscopy method, used to investigate micro-scale objects. Using (often white) light, an object is illuminated, the scattered light is collected through a system of lenses, including an objective lens, and the object is projected either into a set of binoculars or directly into a camera. The resolution of the microscope is dependent on the wavelength (λ) of the light that is used to illuminate the sample, and the numerical aperture (NA): a characteristic of the objective lens indicating the angle at which the lens can accept light. The resolution is then given by[55]

$$d = \frac{\lambda}{2NA}. \tag{3.1}$$

The resolution can be of the order of the wavelength of the light used[56], though in the microscopes used in this work the resolution is of the order of 1 μm - 10 μm.

In this work two illumination methods are used: bright and dark field illumination. In bright field illumination the directly reflected beam (first order scattered beam) is used to image the sample. Any contrast is caused by scattering or absorption of the light, showing dark features on a bright background. In dark field illumination, the first ordered scattered beam is excluded from the image, showing the light scattered by the sample. This highlights edges and scatter centers that may be difficult to see in bright field illumination[57].

3.3.2 Electron microscopy

Scanning electron microscopy

Scanning electron microscopy (SEM) is a microscopy method that can be used to investigate nanostructures with features on the order of 1 nm. When an electron beam is scanned across the surface of a sample, it penetrates into the surface releasing among others high energy back-scattered electrons and secondary electrons. The secondary electrons are electrons that are excited and released from the material after inelastic scattering with the incoming electrons. These secondary electrons usually have low energies and contain information only about the surface, e.g. morphology, of the sample. In a SEM, the beam scans across the surface in a raster, as the secondary electrons are collected for

every raster point. The electron count per raster point is displayed in the form of an image. Typically, the resolution of an SEM is of the order of 10 nm, although resolutions of the order of 1 nm can be achieved[57].

Some SEMs are able to be operated in so called transmission mode, resulting in scanning transmission electron microscopy (STEM). In STEM, it is not the back scattered secondary electrons that are collected, but instead the transmitted, mostly inelastically scattered, electrons are collected behind the sample for every raster point. This means that the sample can not be very thick, as the electrons need to be able to penetrate through the sample. Unlike most SEM images, STEM images can also contain information about the structural properties of the sample. It is, for example, possible to image crystal defects like twin planes in a STEM. The resolution of a STEM is, e.g., dependent on the acceleration voltage of the incoming beam. Dedicated STEM systems in transmission electron microscopes can achieve atomic resolution (see below), but combined SEM/STEM systems have resolutions similar to those of the SEM[57].

Transmission electron microscopy

In transmission electron microscopy (TEM), a similar technique as described above for STEM can be used, but in addition a small area can be illuminated with the electrons and the transmitted electrons are collected after the sample, much like the light in optical microscopy. The acceleration voltage in a TEM system is often larger than in a SEM system, which corresponds to a smaller electron wavelength. While travelling in the sample some electrons are scattered, either elastically on the atomic nuclei, or inelastically on the atomic electrons in the sample[57]. Regardless of the scattering process, the primary beam, that is collected after the sample, will have an intensity variation depending on e.g. the thickness, density and atomic composition of the sample. In crystalline samples, such as III-V semiconductor nanowires, it is possible to achieve atomic resolution in a TEM, where the individual atomic planes are visible. This way it is possible to distinguish between wz and zb crystal structure within the same nanowire.[18]

The process above describes bright field illumination, but similarly to optical microscopy, dark field illumination is possible. In crystalline materials, low angle scattered electrons create a interference pattern. It is possible to filter out all scattered electrons except for the ones contributing to one specific diffraction spot. Considering the fact that the interference pattern is dependent on the crystal structure, this method can be used to highlight specific crystal structures or stacking faults in a material.[57]

Although both TEM and STEM detect electrons transmitted through the sample, they are not the same technique. In TEM an area is illuminated with a collimated beam and the image is recorded using a spatially resolving detector, for example a fluorescent screen. Here the resolution is dependent only on the lens system and the wavelength of the electrons. In STEM or SEM in transmission mode, the beam is focused on the sample and scanned in a raster pattern. The resolution in STEM is dependent on the raster density and the interaction volume of the electron beam in the material. The detection in a STEM system can be a single detector, detecting the integrated intensity of the primary beam passed through the sample at each raster point, or in the case of a more complex detection system, different detectors at different scattering angles, sometimes split up into multiple sections. In both TEM and STEM however, the sample needs to be thin enough for electrons to be transmitted through the sample.[57]

The SEM images in paper I are recorded in a Zeiss Leo Gemini 1560 thermal field emission SEM. The acceleration voltage used is 15 kV. The STEM images in paper II are acquired in a Hitachi SU8010 Cold Field Emission SEM with a separately installed STEM detector. For the STEM images, an acceleration voltage of 30 kV is used. Finally, the TEM images in paper III are taken with a Jeol 3000F field emission TEM at an acceleration voltage of 300 kV.

3.4 One-band effective mass calculations

It is useful to predict the electronic properties of nanoscale semiconductor structures before fabrication or to compare to experimental data. There are many methods of calculating energy levels in confined nanostructures, but one of the simplest methods is solving the time independent Schrödinger equation (see section 2.2.2) for the potential landscape of the semiconductor structure. The potential landscape of a structure, for example a Q-dot, is dependent on the bandgaps and band offsets of the material, but also on the strain in the system if materials with different lattice parameters are used. In addition, the Hamiltonian in equation (2.1) is dependent on the electron mass (if confinement in the conduction band is considered), which may differ between materials. Lastly, in some III-V semiconductors, the valence band is degenerate, meaning that multiple electron bands with different effective masses have their maximum at the valence band maximum. This can complicate calculations.

In order to take these different elements into account, the 3D energy calculations in this work are done with a quasi-empirical method in three steps, according to reference [58]. Firstly, the geometry of the system is defined, then the strain

distribution and finally energy eigenstates are calculated. The geometry of the system is approximated to be perfectly cylindrical, in the case of nanowires, with uniform passivation shells. Q-dots or other segments are defined as insets along the nanowire axis.

The strain distribution is calculated using continuum elastic theory, by minimizing the free energy for a cubic crystal structure. The defined geometry is translated to a cubic grid with a grid spacing smaller than the lattice constants of the materials used. The free energy is then minimized using the conjugate gradient algorithm yielding a strain tensor σ_{ij}. The resulting Hamiltonian used in the time independent Schrödinger equation is then (for the conduction band):

$$\hat{H}_e = E_c - \frac{\hbar}{2m_e}\nabla^2 + a_c\sigma - eV_p \tag{3.2}$$

where E_c is the conduction band energy, m_e is the local effective mass and a_c is the conduction band deformation potential, all of which are material dependent and can vary spatially. σ is the hydrostatic strain, which is the trace of σ_{ij} and V_p is the electrostatic potential which is found by numerically solving Poisson's equation. Because of the degenerate nature of the valence band equation (3.2) is only correct for the conduction band. However, it is possible to use an adjusted version of equation (3.2) for the valence band if an effective mass approximation is used. In quantized systems, the heavy hole valence band will always have the lowest energy, so for the valence band ground state energy, it is possible to use equation (3.2) but E_c becomes E_v, m_e becomes m_{hh} the and a_c becomes a_{hh}.

Finally, to calculate the energy states in the system, a finite difference version of this Hamiltonian is diagonalized using the Lanczos algorithm [59] on the previously defined cubic grid.

It is useful to remember that the calculated values for the energy states may differ from experimental values due to assumptions in the defined geometry as well as errors inherent to numerical methods. For example, the grid spacing plays a role in the calculated energy. While a smaller grid spacing yields more accurate results, it also polynomially increases the calculation time. In addition the method relies on empirical values such as the deformation potential, which means it is reliant on the accuracy of the measurements of these empirical values.

3.5 Sample preparation and procedures

After sample growth, the nanowires are standing, randomly distributed on a growth substrate. To be able to carry out single nanowire PL measurements, they need to be transferred to a different substrate where they are deposited laying on the long edge. The method of transfer is dependent on the type of substrate the nanowires are transferred to, which in turn is dependent on the type of electron microscopy.

If the nanowires are to be invesigated using SEM, they are transferred onto a gold covered Silicon (Si) substrate. The substrates are patterned with a grid, which makes it possible to identify and label single nanowires. Figure 3.3 shows a dark-field optical microscope image of such a substrate with several individual nanowires indicated. The nanowires are mechanically transferred by breaking them off from the substrate and depositing them on the Si substrate with low enough density to identify single nanowires. The individual nanowires are mapped out using dark field optical microscopy, after which they are investigated using μ-PL and finally morphologically and structurally investigated using SEM, STEM or TEM.

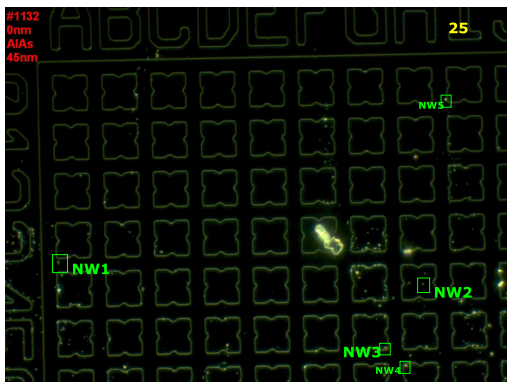

Figure 3.3: A dark field optical microscopy image of a gold covered Si substrate with a pattern to be able to identify single nanowires. Single nanowires are indicated on the substrate using green squares.

For STEM and TEM investigated nanowires, Si TEM grids are used. The grids are covered with a 15 nm film of Silicon Nitride ($Si_{1-x}N$), and have several windows for investigation (see figure 3.4). To transfer the nanowires, a piece of growth substrate is suspended in a small amount of 2-isopropanol in a reaction tube. Using an ultrasonic bath, the nanowires are broken off and suspended in the liquid. A droplet is pipetted onto the SiN-covered substrate and evaporates, leaving behind randomly distributed nanowires on the substrate. Again

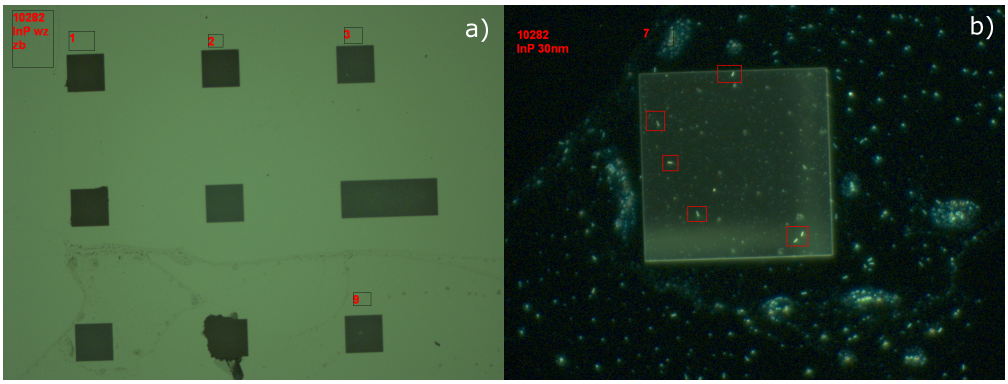

Figure 3.4: A SiN covered Si TEM grid. a) shows a bright field optical microscopy image of all windows of the TEM grid. b) shows a dark field optical microscopy image of a single TEM window. Single nanowires are indicated using red squares.

the nanowires are mapped using dark field optical microscopy (see figure 3.4b) and investigated using μ-PL. Finally the nanowires are structurally investigated using STEM or TEM.

For the PL and PLE measurements, the samples were mounted onto a continuous flow liquid helium cryostat, on which the samples were cooled to approximately 5-7 K. The investigation into radial band bending in GaAs nanowires (Paper I) was done using the 532 nm laser line of a frequency doubled Nd:YAG laser both in tight and side focusing configuration. For the investigations into 2DEGs at wz-zb InP interfaces (Paper II) and crystal phase Q-dots (Paper III), a tunable, optically pumped Ti:Sa laser was used in tight focusing configuration, although it was used at a wavelength of 710 nm for all PL measurements. For the PLE measurements the laser was scanned from 830 nm to 710 nm. The PL was collected trough a 20x objective lens onto a thermoelectrically cooled CCD camera.

All nanowires were investigated using power-dependent PL, in which the EPD is decreased using varying neutral density filters. This way the EPD could be reduced over up to 8 orders of magnitude. To compensate for the reduction in PL intensity, the integration times were increased to up to 2 hours in some cases.

After the PL and PLE measurements, the nanowires were imaged using EM in order to check the individual nanowires for irregularities such as stacking faults and to determine the morphology of the nanowires.

For the work on crystal phase GaAs Q-dots (Paper III) the TEM measurements

were used to determine the size of the Q-dots in order to do one-band effective mass calculations. The parameters used in the calculations are given in table 3.1. Wz-GaAs and zb-GaAs are assumed to have the same lattice constant (a) and hydrostatic strain. Because there have been contrasting reports on the effective masses in wz-GaAs[30,31] the wz-GaAs effective mass is found by fitting the measured wz-GaAs transition energies with the corresponding diameters found by TEM.

Table 3.1: Parameters used in one-band, effective mass calculations of zb GaAs Q-dots in wz-GaAs nanowires.

$E_{g,zb}$	1.519 eV[60]
$E_{g,wz}$	1.517 eV[17,24]
$m_{e,zb}$	0.067 m_0[60]
$m_{hh,zb}$	0.5 m_0[61]
$m_{e,wz}$	0.09 m_0
$m_{hh,wz}$	0.45 m_0[29]
ΔE_v	115 meV[29]
a	0.565 nm[35,60]

The calculations are done on a cubic grid with 0.1 nm gridpoint spacing. The AlAs shell used in the calculations was 10 nm thick. The size of the calculation grid was trimmed to the size of the area of interest, which in this case was the zb-GaAs Q-dot and the wz-GaAs core with 6 nm barrier material on all sides to account for tunneling. To calculate the radial confinement in the conduction and valence band of the wz-GaAs nanowire core, a wz-GaAs cylinder was simulated. This was done on a grid with 0.5 nm gridpoint spacing and $m_{e,wz}$ was varied to match the calculated bandgap transition with the measured values.

Chapter 4

Results

In this chapter I will present the work of the three included articles in more detail. First I will showcase my work on radial band bending at wz-zb interfaces in GaAs nanowires (paper I). Next I will present my work on 2D electron gases at wz-zb InP interfaces (paper II) and finally I will show my work on 0D polytype quantum dots in GaAs nanowires (paper III)

4.1 Radial band bending in GaAs

Chapter 1 went into detail on the use of polytype heterostructures in place of material heterostructures for a few suggested applications. An important feature of heterostructure design in any material system is the valence and conduction band offset between the different materials. In the case of wz-zb semiconductor interfaces discussed in this thesis, the band alignment is type-II which means there is a positive step in the conduction band and a negative step in the valence band. How large this valence band offset (ΔE_v) is can be measured using PL, as explained in section 2.2.3. The band offset between wz and zb GaAs has been reported to be 80-115 meV[14,29,33,34,41], however, there have been indications that the measurements are dependent on the nanowire diameter[29].

As described in section 2.2.3, the energy of the PL from the type-II interface is dependent on the EPD, where the energy is higher for larger EPD. In section 2.3 the principle of Fermi level pinning is described, where the recombination energy is decreased due to radial band bending and the spatial separation of

charge carriers. To investigate the effect of Fermi level pinning on the PL from the type-II interface, excitation power dependent PL measurements were done on GaAs nanowires with a variety of diameters.

The nanowires consisted of zb-GaAs with an insert of wz-GaAs. The nanowires were grown from gold seed particles ranging between 15-75 nm, However, because of the radial overgrowth on the nanowires, the final nanowires ranged between 80-160 nm in diameter. The length of the wz segment was between 30-70 nm, which is large enough not to have any confinement effects in the axial direction. There were two sets of nanowires: a set without a shell and a set radially overgrown with 15 nm of AlAs to investigate the effect of a passivating capping layer. Because AlAs is reactive with oxygen, these nanowires were capped with another 5 nm layer of $Al_xGa_{1-x}As$ with an Al content of approximately 20%-30%. I will refer to the two sets as uncapped and capped, respectively.

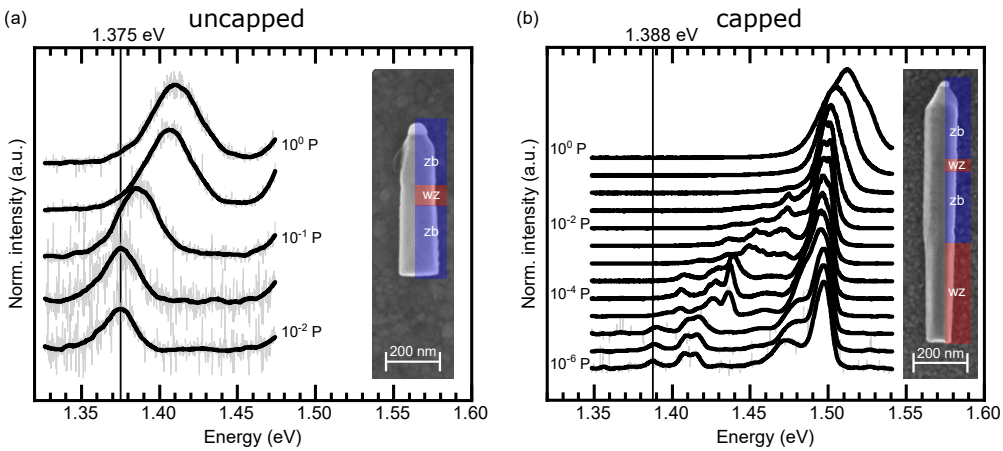

Figure 4.1: Examples of power-dependent PL for a) uncapped wz-zb GaAs nanowires and b) wz-zb GaAs nanowires capped with 15 nm of AlAs and 5 nm of AlGaAs. A SEM image of either nanowire is included in the image.

Figure 4.1a shows typical power dependent PL spectra for an uncapped wz-zb GaAs nanowire. As mentioned in section 1 the bandgap of wz- and zb-GaAs is 1.52 eV at cryo temperature. This would be to the right of the recorded spectrum and only the tail of the bandgap peak is visible. The peak that is visible in the spectrum at 1.41 eV at high EPD is the peak corresponding to the type-II recombination. The decrease of the type-II recombination energy with decreasing EPD is clearly visible. This phenomenon is typical of a type-II interface and is caused by the spatially indirect character of the transition as described in section 2.2.3. The low energy limit of this type-II energy shift

is 1.375 eV for this nanowire with a diameter of 132 nm. At this EPD the triangular quantum wells at the wz-zb interface are depleted and the type-II peak stops red-shifting. The type-II energy at this EPD is called the type-II transition energy ($E_{type-II}$).

The power dependent PL spectra of the capped nanowires are similar. The bandgap peak is visible at high EPD at an energy of 1.52 eV, which then disappears. A dominant impurity related peak at an energy of 1.50 eV is clearly visible at all EPD. At lower EPD small sub-peaks are visible with a red-shifting envelope. These sub-peaks have been visible in similar samples with variable shell thicknesses, as well as very thick (>250 nm diameter) uncapped GaAs nanowires with a single wz-zb interface. We speculate that the sub-peaks are due to the energy levels in the triangular quantum wells at the wz-zb interface. The sub-peaks show a very slight red-shift with lowering EPD, which coincides with the lowering of the triangular well levels due to the decreasing electric field across the type II interface.

In both capped and uncapped nanowires, the low energy limit of the type-II emission is only reachable at very low EPD. At this low EPD, the PL signal is low compared to the background noise. To achieve sufficient signal-to-noise ratio, the integration times were very long, up to several hours for one measurement. For many measured nanowires, the signal-to-noise at low EPD was too low for the type-II emission to reach the type-II transition energy.

In principle the lowest achievable energy of the power dependent PL of a type-II interface is that of the so-called flat band energy: when there are no charge carriers accumulating on either side of the interface and there is no electric field to bend the bands into triangular wells. As we discussed in section 2.2.3 it is not possible to achieve true flat band conditions, because of Fermi-level matching far away from the interface. However, the conditions should still be similar, irrelevant of the diameter of the nanowire and the type-II transition energy should be the same for every nanowire.

However, if we plot the type-II transition energies as a function of the diameter, as in figure 4.2, we see a diameter dependence of the type-II emission. Because of the sub-peaked behaviour of the capped nanowires, we show the diameter dependence for the uncapped nanowires in figure 4.2a while the data for the capped nanowires is shown infigure 4.2b. The plots show in blue the measured type-II transition energies as a function of the nanowire diameter. These are the cases for which the signal-to-noise at low EPD was high enough for the type-II transition energy to be discerned. The grey points show the type-II emission energy for nanowires for which the signal-to-noise was too low to discern the

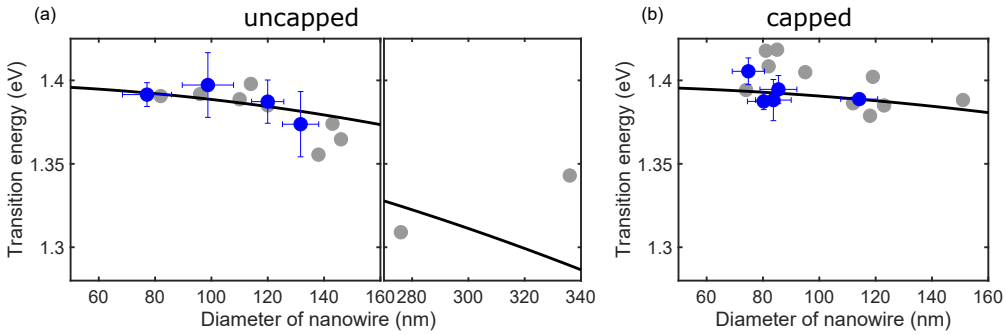

Figure 4.2: The type-II transition energies as a function of the diameter of the a) uncapped and b) capped wz-zb GaAs nanowires.

type-II transition energy. For these nanowires, the type-II transmission energy is lower than or equal to the indicated energy.

A diameter dependence is visible for the transition energies. This is visible both in the capped and uncapped nanowires. This is as expected from the theory in section 2.3. GaAs is known to have a large amount of surface states, which pin the Fermi-level to the surface charge neutral level (ψ_{CNL}). Since the nanowires are grown by MOVPE (see section 3.1), there is carbon incorporation into the nanowire during growth. This means that the nanowires are unintentionally p-doped[51], and at cryo-temperatures the Fermi-level should be close the the acceptor energy level. As is explained in figure 2.12 this difference of Fermi-level causes radial band bending, creating a radial depletion region. For nanowires with a doping level and diameter like those used in this research, the depletion region is larger than the radius of the nanowire and the nanowires are fully depleted. This is even the case for the nanowires with the AlAs/AlGaAs shell. While the capping layer passivates the surface states of the GaAs core, surface states are still expected to exist at the AlGaAs-air interface. The Fermi-level pinning at the AlGaAs surface translates to radial band bending in the GaAs core.

Due to radial band bending there is a separation of charge carriers. In the case of lightly p-type doped nanowires, such as those used in this study, the electrons will collect close to the surface of the nanowire, whereas the holes will collect in the center of the nanowires. When an electron and a hole recombine from these positions, the emitted energy is decreased due to the Franz-Keldysh effect[50,62]. The difference in emitted energy is exactly the build-in potential ψ_{Bi}: the difference in potential between the center of the nanowire and the surface of the nanowire.

By solving the Poisson equation for fully depleted nanowires, an expression for ψ_{Bi} can be obtained. As described in section 2.3.1, ψ_{Bi} is dependent only on the doping N_A and the radius R of the nanowire for fully depleted nanowires. The final type-II transition energy is then given by

$$E_{type-II} = E_g - \Delta - q\psi_{Bi}(R) = E_g - \Delta - \frac{q^2 N_A}{4\varepsilon_s} R, \tag{4.1}$$

where E_g is the bandgap of GaAs, which are similar for wz- and zb-GaAs, ε_s is the permittivity of GaAs and Δ is the observed band offset. An important note is that Δ is different from the actual band offset ΔE_v, since even at low EPD there are triangular wells at the interface due to Fermi-level matching. This means that there is confinement in the wells even at low EPD, decreasing the observed band offset from the actual band offset.

Equation (4.1) was fitted to the data in figure 4.2. This was done separately for the capped and the uncapped nanowires using a weighted fit [63] and only the data with high enough signal-to-noise to determine the type-II transition energy (blue in figure 4.2) was used. The resulting curve is shown as a solid black line in figure 4.2.

From the fit N_A and Δ can be determined. In both the case of capped and uncapped nanowires, we find a doping concentration of $10^{15} - 10^{16}$ cm^{-3}. This is of the order of magnitude to be expected for unintentionally doped GaAs nanowires, and has been reported in the same order of magnitude for similar nanowires [51]. Since Δ is dependent on the confinement in the triangular wells on either side of the wz-zb interface, the shape of these triangular wells needs to be taken into account. The shape of these triangular wells are dependent on the doping concentration and can be calculated by solving the one-dimensional Poisson equation in the axial direction. By subsequently solving the one-dimensional Schrödinger equation, the energy levels and thus the confinement in the wells can be calculated. This allows us to fit ΔE_v to Δ.

Because of differences in the geometry, we calculated the band offset separately for the capped and the uncapped nanowires. We found a band offset of 130 ± 20 meV for the capped nanowires and 120 ± 10 meV for the uncapped nanowires. This is larger than previously reported values [17,33], where the radial band bending and the confinement in the triangular wells was not taken into account. From the calculations we also found an energy level separation of 9 meV for holes, which is of the same order as of the observed peak separation in figure 4.1b.

With this I have demonstrated that the effect of Fermi-level pinning is clearly visible on the optical response of polytype semiconductors with a high density

of surface states, such as in GaAs. This is important to take into account when designing polytype heterostructures for possible applications. Two of such applications are explored below.

4.2 2DEG formation in polytype InP

2D electron gases (2DEGs) are commonly used to study interesting electronic effects such as Wigner crystals[6], and are used in high speed applications such as high electron mobility transistors (HEMTs)[4]. An important necessity in these 2DEG applications is the high mobility of the electron gas[64]. In semiconductors the 2DEG mobility is affected by scattering, such as Coulomb scattering on ionized donors, scattering on phonons and scattering on interface roughness. The first two of these processes can be reduced by modulation doping, doping a distance away from the interface, and cooling of the material. Interface roughness, however, is inherent to material heterostructures, due to strain and intermixing.

This is why I investigated polytype heterostructures as a possible medium for 2DEGs, since they do not have any strain or atom intermixing at the interface and are therefore completely smooth and atomically sharp. In this study wz-zb InP nanowires are used. The nanowires are grown using gold particles that are 30 nm in diameter, but due to radial overgrowth, the diameter of the nanowires varies from 80-200 nm. Two sets of samples are invesigated. One set consist of nominally undoped (unintentionally doped) nanowires with a wz-InP stem and a zb-InP top segment. The other set has the same geometry, but the wz-InP core is doped with sulphur (S), which is n-type doping. Since the wz-zb InP interface has a type-II band alignment with the zb-InP conduction band being lower in energy than the wz-InP conduction band, the electrons from the n-type doping are expected to collect in a triangular well on the zb-InP side of the interface, modulating doping the zb-InP segment.

Figure 4.3 shows power dependent PL measurements for both the undoped and doped nanowires. The PL spectra of an undoped nanowire is shown in figure 4.3a. A STEM image of the nanowire is shown as an inset in the figure, although only the top part of the nanowire is shown in the image. The full nanowire consists of a stem of about 1.5 μm wz-InP and top segment of 200 nm zb-InP. The single interface can be seen in the image by a very faint bright line between the wz and the zb segment.

The PL spectra show a peak at 1.49 eV, which can be attributed to the bandgap emission of wz-InP. A faint peak at 1.42 eV can be identified, which corresponds

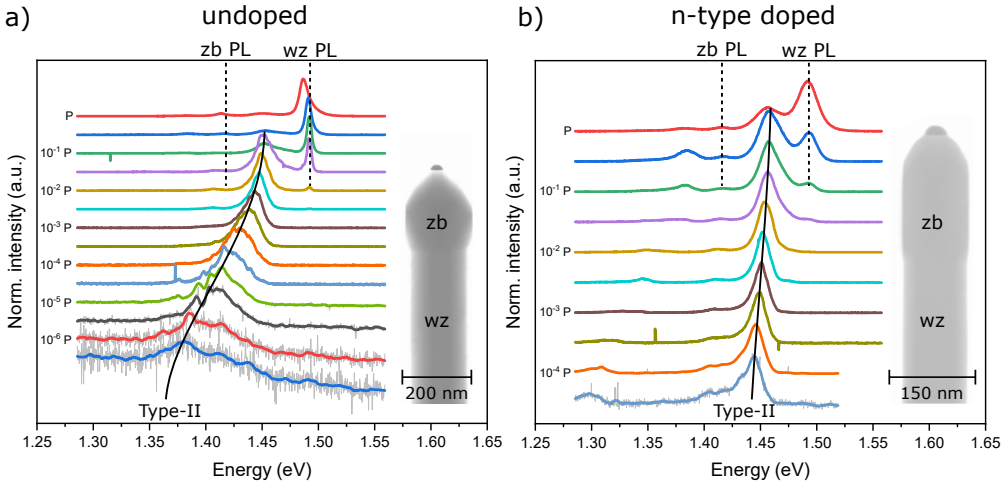

Figure 4.3: Typical power dependent PL-spectra of a) an undoped wz-zb InP nanowire and b) a wz-zb InP nanowire with a doped wz segment. The inset shows in STEM image of the corresponding nanowire.

to the bandgap emission of zb-InP. The difference in bandgap is therefore $\Delta E_g = 70$ meV, which is comparable to previously reported values[20,28,65]. Since the zb-InP segment is about eight times shorter than the wz-InP segment, the intensity difference between the two bandgap emissions is to be expected. The third peak, that becomes visible at 1.45 meV, shows a red-shifting behaviour with lowering EPD. This shift is characteristic of type-II PL and is in detail explained in section 2.2.3. At low EPD the type-II PL shifts to energies below the zb-InP bandgap, which is as expected. However the signal-to-noise ratio is too poor to see the type-II transition energy: the energy at which the type-II PL stops red-shifting, indicating depleted triangular wells at the interface.

Figure 4.3b shows the power dependent PL spectra of an InP nanowire with a single wz-zb interface, of which the core of the wz segment is n-type doped. Again a PL signal of wz- and zb-InP can be identified. The type-II shifting peak can also be indentified. It is clear to see that, although a slight red-shift is visible for the type-II recombination with lowering EPD, the shift is much less pronounced in the undoped case.

The reason for this is schematically given in figure 4.4. For high EPD, the triangular wells at either side of the interface are filled with generated charge carriers. The recombination is therefore high in energy: higher than the zb bandgap, but lower than the wz bandgap. This is the same for both the doped and undoped nanowires. For the undoped nanowire, at low EPD both triangular wells deplete

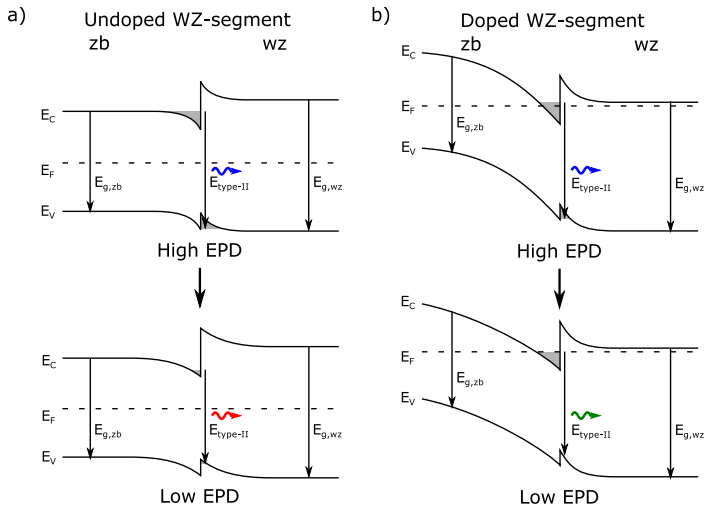

Figure 4.4: A schematic representation of the type-II recombination across the wz-zb InP interface at high and low EPD for a) an undoped wz-zb InP nanowire and b) a wz-zb InP nanowire with a n-type doped wz segment.

and thus the recombination energy decreases to below the zb bandgap. For the doped nanowires, however, the electron triangular well remains populated due to the modulation doping. In this case only the hole triangular well depletes of its charge carriers with decreasing EPD, which means that the recombination will have a higher energy compared to the type-II recombination of the undoped nanowires. This not only explains the observed difference between the doped and undoped nanowires in this study, it also shows it is possible to create a 2DEG using modulation doping at an atomically sharp wz-zb interface.

It is noteworthy that, unlike the GaAs nanowires in section 4.1, the PL signal of neither the doped nor undoped nanowires reaches the type-II transition energy and stops shifting at low EPD. This is due to the low signal-to-noise ratio at low EPD. Therefore it is not possible to find the valence band offset between wz- and zb-InP directly from the emission energy.

Another noteworthy feature of the PL spectra in figure 4.3 is the type-II emission energy at high EPD (for ease denoted with E_{hp}). E_{hp} for the undoped nanowires is lower compared to the modulation doped nanowires for all measured nanowires. While the doped nanowire has $E_{hp} = 1.47$ eV, the undoped nanowire has only $E_{hp} = 1.45$ eV. To understand why, we need to look at the shape of the bands at high EPD more closely, which are shown in figure 4.5.

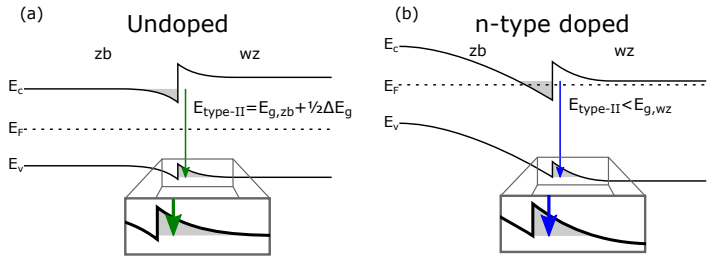

Figure 4.5: A schematic representation of an intrinsic and a n-type doped wz-zb InP interface at high EPD. The triangular well depth for an n-type doped wz-zb inP interface is larger, so the recombination energy across the type-II interface will also be larger for the n-type doped case.

The Fermi level in an nominally undoped nanowire is positioned in the middle of the band gap. With this knowledge, it is possible to calculate the depth of the triangular wells on either side of the wz-zb InP interface, and thus to calculate the expected E_{hp}. Assuming the triangular wells are completely filled both for the electron and hole well, and making the assumption that $\Delta E_v > \frac{1}{2}\Delta E_g$, this turns out to be exactly $E_{hp} = E_{g,zb} + \frac{1}{2}\Delta E_g = 1.455$ eV, right in the middle between the zb-InP and wz-InP bandgap energy. In all measured undoped nanowires the E_{hp} is exactly on or slightly below that calculated energy.

For the modulation doped nanowires, the Fermi-level is close to the conduction band in the wz-InP segment, but since the zb-InP segment is undoped the Fermi-level on the zb side of the interface will be in the middle of the bandgap. This creates strong band bending near the interface, resulting in deeper triangular wells. Again the depth of the wells can be calculated. Now, if we again assume complete filling of the hole triangular well and that $\Delta E_v < \Delta E_g$, we find that the transition energy at high EPD becomes $E_{g,zb} + \frac{1}{2}\Delta E_g < E_{hp} < E_{g,wz}$. This is larger than in the undoped case and is observed in all measured modulation doped InP nanowires in this study

It is also important to note that if, in the case of the doped nanowires, one was to assume $\Delta E_v > \Delta E_g$, the high EPD transition energy would be $E_{hp} = E_{g,wz}$. This has not been observed in any of the samples in this study, so this suggests that the valence band offset between wz- and zb-InP is $\frac{1}{2}\Delta E_g$ =35 meV< $\Delta E_v \leq \Delta E_g$ =70 meV. This is in good agreement with calculated values [14,34,41].

While it is, in this way, possible to explain quantitatively the high EPD behavior of the type-II emission of undoped and n-type doped wz-zb InP nanowires, many assuptions have to be made in the process. Firstly, this assumes a sufficiently high doping in the wz-InP segment, so that the Fermi-level is not affected by the

optical generation of charge carriers. And secondly, this also assumes uniform doping in the whole nanowire. This last point is untrue, since growth of an undoped shell occurs simultaneously as the growth of the undoped zb-InP segment. Despite these limitations it is possible to determine an upper and lower limit of the valence band offset between wz-zb InP.

4.3 Crystal phase defined GaAs quantum dots

Besides 2DEGs, polytype heterostructures are also good candidates for well defined, 0-dimensional Q-dots, due to their atomically sharp interfaces. Photon correlation experiments show promising results for the use of polytype heterostructures as single photon sources[66,67]. However, before polytype Q-dots can be used in any applications, good control on the amount and dimensions of the Q-dots, as well as their characterization, is necessary.

For this reason I investigated zb-GaAs Q-dots embedded in radially confined wz-GaAs nanowires. Each nanowire contained exactly one dot, with diameters ranging from 15-25 nm and lengths between 10-20 nm. To improve PL yield and reduce surface effects, each nanowire was capped with an approximately 20 nm thick AlAs shell, which again was passivated with an AlGaAs shell. While the nanowires are not actively doped, an unintentional doping of 10^{15}-10^{16} cm^{-3} is expected, comparable to the nanowires used in section 4.1. With this doping level, the nanowires are expected to be fully depleted due to Fermi-level pinning, but since the diameter is so small, the radial confinement is expected to be much larger than the influence of Fermi-level pinning.

As was described in reference[17], when growing a AlAs shell, there often forms a zb-AlGaAs segment in the axial direction. Since the Al content at this interface is unknown, the properties of this wz-zb GaAs/AlGaAs interface are also unknown. In order to have more control over this specific interface, a zb-GaAs segment was grown before the AlAs shell, creating a wz-zb GaAs interface in addition to the original zb-GaAs Q-dot. A set of reference nanowires are grown that contain only the wz-zb GaAs interface at the top of the nanowire, in order to distinguish between the PL signal from the Q-dot and the interface.

Figure 4.6a shows the power dependent PL spectra and the PLE spectrum of the nanowire shown in figures 4.6b and c. The nanowire has a core diameter of 16.6 nm and the zb-GaAs Q-dot has a length of 13 nm. At high EPD, the PL spectra show the wz-GaAs bandgap emission at 1.547 eV, which is echoed in the PLE spectrum by a sharp increase in signal at 1.55 eV. At low EPD,

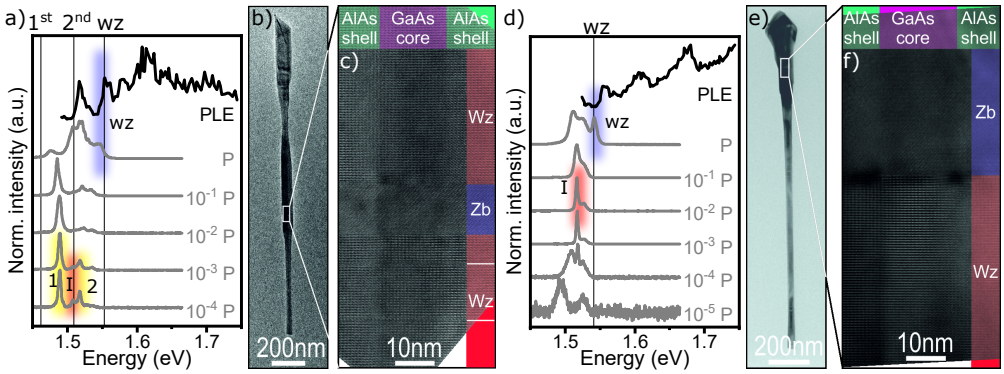

Figure 4.6: Photoluminescence spectra of the Q-dot and reference samples. a) The normalized PLE spectrum and power dependent PL spectra of a nanowire containing a Q-dot. The wz-GaAs band-to-band emission, first and second Q-dot emissions, and the emission from the wz-zb GaAs interface are labeled wz (blue), 1 and 2 (yellow), and I (red) respectively. The calculated transition energies for the first and second dot state, as well as the wz-GaAs band-to-band emission, are indicated with black lines. b) and c) show a bright field and a high resolution TEM image of the nanowire containing the Q-dot, respectively. d) The normalized PLE spectrum and power dependent PL spectra of a nanowire with a single wz-zb GaAs interface. The wz-GaAs band-to-band emission and the emission from the interface are labeled wz (blue) and I (red) respectively. The calculated transition energy for the wz-GaAs band-to-band emission, is indicated with a black line. e) and f) show a bright field and a high resolution TEM image of the nanowire containing a wz-zb GaAs interface, respectively.

three peaks are visible at 1.489 eV, 1.508 eV and 1.518 eV. I attribute these peaks to the emission from the first Q-dot level, the wz-zb interface and the second Q-dot level respectively. This is confirmed by PLE. The PLE spectrum is recorded with the detection window overlapping with the emission from the first Q-dot level (labeled 1 in figure 4.6a). Besides the aforementioned wz-GaAs bandedge, the PLE also shows a 0D DOS at 1.52 eV, overlapping in energy with the emission from the second Q-dot level (labeled 2 in figure 4.6a).

Note that the PLE spectrum does not show any increased signal when the excitation energy overlaps with the wz-zb GaAs interface emission peak, labeled I in figure 4.6a. This indicates that this emission indeed originates from a different, isolated source in the nanowire, in this case the wz-zb GaAs interface.

The vertical black lines in figure 4.6a indicate calculated values for the 1st and 2nd energy level in the Q-dot, as well as the wz-GaAs bandgap transition. The calculations are done using the geometric measurements extracted from the TEM images. The calculated values give reasonable overlap with the measured PL and PLE spectra. The difference between the calculated and measured values can be attributed to the simulations made in the calculation process.

Figure 4.6d shows the power dependent PL spectra, as well as the PLE spectrum, of a nanowire containing only a single wz-zb GaAs interface, as shown in figures 4.6e and f. The considered nanowire has a core diameter of 20.7 nm. The high EPD PL spectra again show the wz-GaAs bandgap emission, this time at 1.548 eV. When the EPD is decreased a singular sharp peak becomes visible with an energy of 1.521 eV. This is again attributed to the wz-zb GaAs interface. The calculated value for the wz-GaAs bandgap emission is indicated with the black line.

The PLE spectrum in figure 4.6d shows the wz-GaAs band edge at 1.55 eV, the second conduction band edge at 1.60 eV and the second valence band edge at 1.68 eV. Since the PLE is recorded with the detection window overlapping with the wz-zb GaAs interface emission, it is not possible to find the DOS at the emission energy. There is, however, a small decrease in PLE intensity at 1.52, indicating a dot-like DOS at the wz-zb interface. This implies that the triangular wells at the wz-zb GaAs interface form Q-dots when the diameter of the nanowire is reduced.

When the EPD of the power dependent PL on the reference sample is further reduced, the sharp interface emission disappears and a broad, red-shifting emission appears. It is unclear where this arises from.

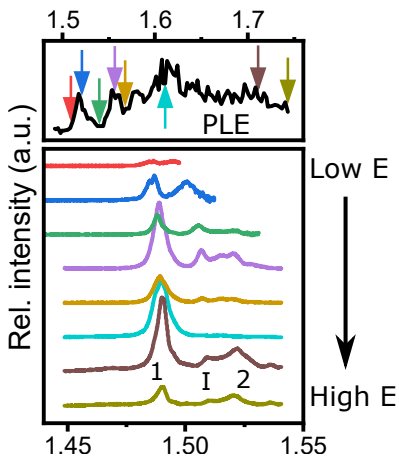

Figure 4.7: PL spectra of the first and second Q-dot states and the interface at different excitation energies. The excitation energy for each spectrum is indicated by a colored arrow in the included PLE spectrum.

Figure 4.7 shows the Q-dot and interface emission of the nanowire shown in figures 4.6b and c at different excitation energies. The colored arrows in the PLE spectrum indicate the excitation energy of the corresponding colored spectrum.

Again, the first and second Q-dot transitions and the emission from the wz-zb interface are labelled 1, 2 and I, respectively. An increase in intensity of the first Q-dot transition is visible when the excitation energy accesses the second Q-dot transition, which is to be expected. Emission from the second Q-dot state, however, does not appear until the wz-GaAs Q-wire states are accessed at 1.55 eV (purple line). This can be explained by state filling: when the wz-GaAs bands become available, more charge carriers are being generated. The generated electrons will fill up the first energy level in the zb-GaAs Q-dot and when it is completely filled, the second Q-dot level will be filled. This would also explain the varying intensity of the second Q-dot transition depending on available DOS at a certain excitation energy. It is important to note that the intensity of the wz-zb interface again behaves independently of the Q-dot transitions.

Interestingly, at an excitation energy of 1.61 eV (cyan line), the emission from both the wz-zb interface as well as from the second Q-dot state completely disappear while the emission from the first Q-dot state remains relatively high. It is unclear why this happens.

Chapter 5

Conclusions and outlook

Polytype heterostructures have multiple advantages over material heterostructures, due to the atomically sharp and unstrained nature of the interface between the different crystal phases. In GaAs and InP, wz-zb interfaces have a type-II band alignment, which makes them good candidates for several applications, a few of which are mentioned in this work.

In this work I have focused on three main topics investigating three different polytype heterostructures. Firstly I investigated the wz-zb GaAs interface properties in nanowires with different diameters. I found that the energy of the photoluminescence from the type-II wz-zb GaAs interface is dependent on the diameter of the nanowire. For larger diameter nanowires a lower type-II photoluminescence energy is recorded, which I attribute to radial band bending due to Fermi-level pinning at the surface of the nanowire. By fitting an analytical model of radial band bending to the data an unintentional doping concentration of $10^{15} - 10^{16}$ cm^{-3} was found, which is comparable to previously reported values. To passivate the surface, an AlAs and AlGaAs radial shell was used. Depite this passivation of the surface states, a radial dependence of the measured type-II PL energy was found. This indicates that there is still Fermi-level pinning at the AlGaAs-air interface, which translates into radial band bending in the GaAs nanowire core. Using the fit of the analytical model, as well as solving the Poisson equation in the axial direction, the band offset is calculated to be 130 ± 20 meV for the data set without a passivation shell and 120 ± 10 meV for the data set with a passivation shell.

The second part of this work focuses on modulation doped wz-zb InP interfaces. I found that the type-II photoluminescence energy is higher when modulation n-

type doping is used. This is attributed to state filling in the triangular potential well, due to a 2DEG residing at the zb-InP side of the type-II interface: the free electrons stemming from incorporated dopants migrate from the wz-InP to the zb-InP and fill the triangular potential well formed in the conduction band at the interface, even when a low EPD is used. I also determined the valence band offset between wz- and zb-InP to be between 35 meV to 70 meV. A 2DEG at such an atomically sharp polytype interface could be desirable in applications where high mobility electron gases are required, due to the lack scattering on interface roughness.

Lastly I investigated crystal phase Q-dots in GaAs. The zb-GaAs Q-dots in the radially confined wz-GaAs nanowires contained two energy levels with a sharp DOS. Besides the zb-GaAs Q-dot, the radially confined wz-zb GaAs interface also showed a sharp photoluminescence signal indicating a sharp DOS. This implies the existance of Q-dot like states at the type-II interface in radially confined nanowires. The calculations, using a simple one band model, are in good agreement with the measured values when a wz-GaAs effective electron mass of $m_e = 0.09m_e$ is used, allowing for simple but fast calculations of expected electronic properties for crystal phase Q-dots.

These results lay the foundation for the investigation for many interesting physical phenomena. Because of the atomically sharp and strainless nature of crystal phase interfaces, the electron, hole or exciton gasses residing at the interface are expected to have high mobilities. Therefore it may be possible for exotic exciton and electron crystals, such as Wigner crystals, to form at the type-II interface. In order to research these phenomena large wz-zb interfaces are necessary, requiring advanced III-V semiconductor growth.

Besides exciton and electron crystals, crystal phase heterostructures can also be used to investigate interesting Quantum mechanical energy states such as ring states. Using a multi-shell GaAs and AlAs structure, it is possible to create crystal phase defined Q-rings. The optical studies and calculations in this work would aid with the understanding of these, as well as other more advanced polytype heterostructures.

Bibliography

[1] M. P. Paranthaman, W. Wong-Ng, and R. N. Bhattacharya, eds., *Semiconductor Materials for Solar Photovoltaic Cells*, vol. 218 of *Springer Series in Materials Science*. Cham: Springer International Publishing, 2016.

[2] R. Braunstein, "Radiative Transitions in Semiconductors," *Physical Review*, vol. 99, pp. 1892–1893, Sept. 1955.

[3] J. Bardeen and W. H. Brattain, "The Transistor, A Semi-Conductor Triode," *Physical Review*, vol. 74, pp. 230–231, July 1948.

[4] T. Mimura, S. Hiyamizu, T. Fujii, and K. Nanbu, "A New Field-Effect Transistor with Selectively Doped GaAs/n-AlGaAs Heterojunctions," *Japanese Journal of Applied Physics*, vol. 19, pp. L225–L227, May 1980.

[5] M. A. Reed, "Spatial quantization in GaAs–AlGaAs multiple quantum dots," *Journal of Vacuum Science & Technology B: Microelectronics and Nanometer Structures*, vol. 4, p. 358, Jan. 1986.

[6] Y. P. Monarkha and V. E. Syvokon, "A two-dimensional Wigner crystal (Review Article)," *Low Temperature Physics*, vol. 38, pp. 1067–1095, Dec. 2012.

[7] W. Zulehner, "Czochralski growth of silicon," *Journal of Crystal Growth*, vol. 65, pp. 189–213, Dec. 1983.

[8] S. M. Sze and K. K. Ng, *Physics of semiconductor devices*. John wiley & sons, 2006.

[9] C. F. Klingshirn, *Semiconductor optics*. Berlin ; New York: Springer, 3rd ed ed., 2007. OCLC: ocm75927377.

[10] M. Sparks and G. K. Teal, "Method of making p-n junctions in semiconductor materials," Mar. 1953.

[11] U. W. Pohl, *Epitaxy of Semiconductors: Introduction to Physical Principles*. Springer Science & Business Media, 2013.

[12] R. S. Wagner and W. C. Ellis, "Vapor-liquid-solid mechanism of single crystal growth," *Applied Physics Letters*, vol. 4, pp. 89–90, Mar. 1964.

[13] M. Koguchi, H. Kakibayashi, M. Yazawa, K. Hiruma, and T. Katsuyama, "Crystal Structure Change of GaAs and InAs Whiskers from Zinc-Blende to Wurtzite Type," *Japanese Journal of Applied Physics*, vol. 31, pp. 2061–2065, July 1992.

[14] A. De and C. E. Pryor, "Predicted band structures of III-V semiconductors in the wurtzite phase," *Physical Review B*, vol. 81, p. 155210, Apr. 2010.

[15] H. J. Joyce, J. Wong-Leung, Q. Gao, H. H. Tan, and C. Jagadish, "Phase Perfection in Zinc Blende and Wurtzite III-V Nanowires Using Basic Growth Parameters," *Nano Letters*, vol. 10, pp. 908–915, Mar. 2010.

[16] S. Lehmann, J. Wallentin, D. Jacobsson, K. Deppert, and K. A. Dick, "A General Approach for Sharp Crystal Phase Switching in InAs, GaAs, InP, and GaP Nanowires Using Only Group V Flow," *Nano Letters*, vol. 13, pp. 4099–4105, Sept. 2013.

[17] N. Vainorius, D. Jacobsson, S. Lehmann, A. Gustafsson, K. A. Dick, L. Samuelson, and M.-E. Pistol, "Observation of type-II recombination in single wurtzite/zinc-blende GaAs heterojunction nanowires," *Physical Review B*, vol. 89, p. 165423, Apr. 2014.

[18] S. Lehmann, D. Jacobsson, K. Deppert, and K. A. Dick, "High crystal quality wurtzite-zinc blende heterostructures in metal-organic vapor phase epitaxy-grown GaAs nanowires," *Nano Research*, vol. 5, pp. 470–476, July 2012.

[19] C.-Y. Yeh, Z. W. Lu, S. Froyen, and A. Zunger, "Zinc-blende–wurtzite polytypism in semiconductors," *Physical Review B*, vol. 46, pp. 10086–10097, Oct. 1992.

[20] Z. Su, N. Wang, H. H. Tan, and C. Jagadish, "2D Carrier Localization at the Wurtzite-Zincblende Interface in Novel Layered InP Nanomembranes," *ACS Photonics*, vol. 8, pp. 1735–1745, June 2021.

[21] M. De Luca, A. Polimeni, M. Capizzi, A. J. Meaney, P. C. M. Christianen, J. K. Maan, F. Mura, S. Rubini, and F. Martelli, "Determination of Exciton Reduced Mass and Gyromagnetic Factor of Wurtzite (InGa)As Nanowires

by Photoluminescence Spectroscopy under High Magnetic Fields," *ACS Nano*, vol. 7, pp. 10717–10725, Dec. 2013.

[22] M. Nilsson, I.-J. Chen, S. Lehmann, V. Maulerova, K. A. Dick, and C. Thelander, "Parallel-Coupled Quantum Dots in InAs Nanowires," *Nano Letters*, vol. 17, pp. 7847–7852, Dec. 2017.

[23] L. Francaviglia, G. Tütüncüoglu, F. Matteini, and A. F. i. Morral, "Tuning adatom mobility and nanoscale segregation by twin formation and polytypism," *Nanotechnology*, vol. 30, p. 054006, Feb. 2019.

[24] B. Ketterer, M. Heiss, E. Uccelli, J. Arbiol, and A. Fontcuberta i Morral, "Untangling the Electronic Band Structure of Wurtzite GaAs Nanowires by Resonant Raman Spectroscopy," *ACS Nano*, vol. 5, pp. 7585–7592, Sept. 2011.

[25] S. Pournia, S. Linser, G. Jnawali, H. E. Jackson, L. M. Smith, A. Ameruddin, P. Caroff, J. Wong-Leung, H. H. Tan, C. Jagadish, and H. J. Joyce, "Exploring the band structure of Wurtzite InAs nanowires using photocurrent spectroscopy," *Nano Research*, vol. 13, pp. 1586–1591, June 2020.

[26] A. Mishra, L. V. Titova, T. B. Hoang, H. E. Jackson, L. M. Smith, J. M. Yarrison-Rice, Y. Kim, H. J. Joyce, Q. Gao, H. H. Tan, and C. Jagadish, "Polarization and temperature dependence of photoluminescence from zincblende and wurtzite InP nanowires," *Applied Physics Letters*, vol. 91, p. 263104, Dec. 2007.

[27] N. Vainorius, S. Lehmann, and M.-E. Pistol, "Non-resonant Raman scattering of wurtzite GaAs and InP nanowires," *Optics express*, vol. 28, no. 8, pp. 11016–11022, 2020.

[28] T. T. T. Vu, T. Zehender, M. A. Verheijen, S. R. Plissard, G. W. G. Immink, J. E. M. Haverkort, and E. P. A. M. Bakkers, "High optical quality single crystal phase wurtzite and zincblende InP nanowires," *Nanotechnology*, vol. 24, p. 115705, Mar. 2013.

[29] N. Vainorius, S. Lehmann, D. Jacobsson, L. Samuelson, K. A. Dick, and M.-E. Pistol, "Confinement in Thickness-Controlled GaAs Polytype Nanodots," *Nano Letters*, vol. 15, pp. 2652–2656, Apr. 2015.

[30] N. Vainorius, S. Lehmann, A. Gustafsson, L. Samuelson, K. A. Dick, and M.-E. Pistol, "Wurtzite GaAs Quantum Wires: One-Dimensional Subband Formation," *Nano Letters*, vol. 16, pp. 2774–2780, Apr. 2016.

[31] M. De Luca, S. Rubini, M. Felici, A. Meaney, P. C. M. Christianen, F. Martelli, and A. Polimeni, "Addressing the Fundamental Electronic Properties of Wurtzite GaAs Nanowires by High-Field Magneto-Photoluminescence Spectroscopy," *Nano Letters*, vol. 17, pp. 6540–6547, Nov. 2017.

[32] M. De Luca and A. Polimeni, "Electronic properties of wurtzite-phase InP nanowires determined by optical and magneto-optical spectroscopy," *Applied Physics Reviews*, vol. 4, p. 041102, Dec. 2017.

[33] M. Heiss, S. Conesa-Boj, J. Ren, H.-H. Tseng, A. Gali, A. Rudolph, E. Uccelli, F. Peiró, J. R. Morante, D. Schuh, E. Reiger, E. Kaxiras, J. Arbiol, and A. Fontcuberta i Morral, "Direct correlation of crystal structure and optical properties in wurtzite/zinc-blende GaAs nanowire heterostructures," *Physical Review B*, vol. 83, p. 045303, Jan. 2011.

[34] A. Belabbes, C. Panse, J. Furthmüller, and F. Bechstedt, "Electronic bands of III-V semiconductor polytypes and their alignment," *Physical Review B*, vol. 86, p. 075208, Aug. 2012.

[35] D. Jacobsson, F. Yang, K. Hillerich, F. Lenrick, S. Lehmann, D. Kriegner, J. Stangl, L. R. Wallenberg, K. A. Dick, and J. Johansson, "Phase Transformation in Radially Merged Wurtzite GaAs Nanowires," *Crystal Growth & Design*, vol. 15, pp. 4795–4803, Oct. 2015.

[36] J. H. Davies, *The physics of low-dimensional semiconductors: an introduction*. Cambridge university press, 1998.

[37] H. Temkin, B. V. Dutt, and W. A. Bonner, "Photoluminescence study of native defects in InP," *Applied Physics Letters*, vol. 38, pp. 431–433, Mar. 1981.

[38] G. Hirt, D. Hofmann, F. Mosel, N. Schäfer, and G. Müller, "Compensation mechanisms in nominally undoped semi-insulating InP and comparison with undoped InP grown under stoichiometry control," *Journal of Electronic Materials*, vol. 20, pp. 1065–1068, Dec. 1991.

[39] J. Wallentin and M. T. Borgström, "Doping of semiconductor nanowires," *Journal of Materials Research*, vol. 26, pp. 2142–2156, Sept. 2011.

[40] E. T. Yu, J. O. McCaldin, and T. C. McGill, "Band Offsets in Semiconductor Heterojunctions," in *Solid State Physics* (H. Ehrenreich and D. Turnbull, eds.), vol. 46, pp. 1–146, Academic Press, Jan. 1992.

[41] M. Murayama and T. Nakayama, "Chemical trend of band offsets at wurtzite/zinc-blende heterocrystalline semiconductor interfaces," *Physical Review B*, vol. 49, pp. 4710–4724, Feb. 1994.

[42] E. Schrödinger, "An Undulatory Theory of the Mechanics of Atoms and Molecules," *Physical Review*, vol. 28, pp. 1049–1070, Dec. 1926.

[43] E. J. Caine, S. Subbanna, H. Kroemer, J. L. Merz, and A. Y. Cho, "Staggered-lineup heterojunctions as sources of tunable below-gap radiation: Experimental verification," *Applied Physics Letters*, vol. 45, pp. 1123–1125, Nov. 1984.

[44] K. Pemasiri, M. Montazeri, R. Gass, L. M. Smith, H. E. Jackson, J. Yarrison-Rice, S. Paiman, Q. Gao, H. H. Tan, C. Jagadish, X. Zhang, and J. Zou, "Carrier Dynamics and Quantum Confinement in type II ZB-WZ InP Nanowire Homostructures," *Nano Letters*, vol. 9, pp. 648–654, Feb. 2009.

[45] H. Kroemer and G. Griffiths, "Staggered-lineup heterojunctions as sources of tunable below-gap radiation: Operating principle and semiconductor selection," *IEEE Electron Device Letters*, vol. 4, pp. 20–22, Jan. 1983.

[46] W. E. Spicer, P. W. Chye, P. R. Skeath, C. Y. Su, and I. Lindau, "New and unified model for Schottky barrier and III–V insulator interface states formation," *Journal of Vacuum Science and Technology*, vol. 16, no. 5, pp. 1422–1433, 1979.

[47] W. E. Spicer, I. Lindau, P. Skeath, C. Y. Su, and P. Chye, "Unified Mechanism for Schottky-Barrier Formation and III-V Oxide Interface States," *Physical Review Letters*, vol. 44, pp. 420–423, Feb. 1980.

[48] H. J. Joyce, S. A. Baig, P. Parkinson, C. L. Davies, J. L. Boland, H. H. Tan, C. Jagadish, L. M. Herz, and M. B. Johnston, "The influence of surfaces on the transient terahertz conductivity and electron mobility of GaAs nanowires," *Journal of Physics D: Applied Physics*, vol. 50, p. 224001, June 2017.

[49] A. C. E. Chia and R. R. LaPierre, "Analytical model of surface depletion in GaAs nanowires," *Journal of Applied Physics*, vol. 112, p. 063705, Sept. 2012.

[50] A. Cavallini, L. Polenta, M. Rossi, T. Stoica, R. Calarco, R. J. Meijers, T. Richter, and H. Lüth, "Franz-Keldysh Effect in GaN Nanowires," *Nano Letters*, vol. 7, pp. 2166–2170, July 2007.

[51] M. Hjort, S. Lehmann, J. Knutsson, R. Timm, D. Jacobsson, E. Lundgren, K. Dick, and A. Mikkelsen, "Direct Imaging of Atomic Scale Structure and Electronic Properties of GaAs Wurtzite and Zinc Blende Nanowire Surfaces," *Nano Letters*, vol. 13, pp. 4492–4498, Sept. 2013.

[52] W. Seifert, M. Borgström, K. Deppert, K. A. Dick, J. Johansson, M. W. Larsson, T. Mårtensson, N. Sköld, C. Patrik T. Svensson, B. A. Wacaser, L. Reine Wallenberg, and L. Samuelson, "Growth of one-dimensional nanostructures in MOVPE," *Journal of Crystal Growth*, vol. 272, pp. 211–220, Dec. 2004.

[53] D. Jacobsson, F. Panciera, J. Tersoff, M. C. Reuter, S. Lehmann, S. Hofmann, K. A. Dick, and F. M. Ross, "Interface dynamics and crystal phase switching in GaAs nanowires," *Nature*, vol. 531, pp. 317–322, Mar. 2016.

[54] G. B. Stringfellow, *Organometallic vapor-phase epitaxy: theory and practice*. Elsevier, 1999.

[55] B. E. A. Saleh and M. C. Teich, *Fundamentals of Photonics*. John Wiley & Sons, Feb. 2019.

[56] E. G. van Putten, D. Akbulut, J. Bertolotti, W. L. Vos, A. Lagendijk, and A. P. Mosk, "Scattering Lens Resolves Sub-100 nm Structures with Visible Light," *Physical Review Letters*, vol. 106, p. 193905, May 2011.

[57] R. F. Egerton, *Physical principles of electron microscopy*. Springer, 2005.

[58] C. Pryor, M.-E. Pistol, and L. Samuelson, "Electronic structure of strained $InP/Ga_{0.51}In_{0.49}P$ quantum dots," *Physical Review B*, vol. 56, pp. 10404–10411, Oct. 1997.

[59] C. Lanczos, "An iteration method for the solution of the eigenvalue problem of linear differential and integral operators," *Journal of Research of the National Bureau of Standards*, vol. 45, p. 255, Oct. 1950.

[60] I. Vurgaftman, J. R. Meyer, and L. R. Ram-Mohan, "Band parameters for III–V compound semiconductors and their alloys," *Journal of Applied Physics*, vol. 89, pp. 5815–5875, June 2001.

[61] W. Nakwaski, "Effective masses of electrons and heavy holes in GaAs, InAs, AlAs and their ternary compounds," *Physica B: Condensed Matter*, vol. 210, pp. 1–25, Apr. 1995.

[62] P. Y. Yu and M. Cardona, *Fundamentals of semiconductors: physics and materials properties*. Springer, 2010.

[63] D. York, N. M. Evensen, M. L. Martınez, and J. De Basabe Delgado, "Unified equations for the slope, intercept, and standard errors of the best straight line," *American Journal of Physics*, vol. 72, pp. 367–375, Mar. 2004.

[64] H. J. Joyce, P. Parkinson, N. Jiang, C. J. Docherty, Q. Gao, H. H. Tan, C. Jagadish, L. M. Herz, and M. B. Johnston, "Electron Mobilities Approaching Bulk Limits in "Surface-Free" GaAs Nanowires," *Nano Letters*, vol. 14, pp. 5989–5994, Oct. 2014.

[65] M. Mattila, T. Hakkarainen, M. Mulot, and H. Lipsanen, "Crystal-structure-dependent photoluminescence from InP nanowires," *Nanotechnology*, vol. 17, pp. 1580–1583, Mar. 2006.

[66] N. Akopian, G. Patriarche, L. Liu, J.-C. Harmand, and V. Zwiller, "Crystal Phase Quantum Dots," *Nano Letters*, vol. 10, pp. 1198–1201, Apr. 2010.

[67] B. Loitsch, J. Winnerl, G. Grimaldi, J. Wierzbowski, D. Rudolph, S. Morkötter, M. Döblinger, G. Abstreiter, G. Koblmüller, and J. J. Finley, "Crystal Phase Quantum Dots in the Ultrathin Core of GaAs–AlGaAs Core–Shell Nanowires," *Nano Letters*, vol. 15, pp. 7544–7551, Nov. 2015.

Printed by Media-Tryck, Lund 2021 NORDIC SWAN ECOLABEL 3041 0903

Lund University
Faculty of Engineering
Department of Solid State Physics

ISBN 978-91-8039-002-6